BBA - Bioenergetics 1865 (2024) 149027

Contents lists available at ScienceDirect

BBA - Bioenergetics

journal homepage: www.elsevier.com/locate/bbabio

Performance of TMRM and Mitotrackers in mitochondrial morphofunctional analysis of primary human skin fibroblasts

Shruti Desai [a,1], Sander Grefte [b,1], Els van de Westerlo [a], Susette Lauwen [a], Angela Paters [a], Jochen H.M. Prehn [c], Zhuohui Gan [b], Jaap Keijer [b], Merel J.W. Adjobo-Hermans [a], Werner J.H. Koopman [b,d,*]

[a] Department of Medical BioSciences, Radboud Center for Mitochondrial Medicine, Radboud University Medical Center, Nijmegen, the Netherlands
[b] Human and Animal Physiology, Wageningen University & Research, Wageningen, the Netherlands
[c] Department of Physiology and Medical Physics and SFI FutureNeuro Centre, RCSI University of Medicine and Health Sciences, Dublin 2, Ireland
[d] Department of Pediatrics, Amalia Children's Hospital, Radboud Center for Mitochondrial Medicine, Radboud University Medical Center, Nijmegen, the Netherlands

ARTICLE INFO

Keywords:
TMRM
Mitotracker
FCCP
Flickering
Mitochondrial morphology

ABSTRACT

Mitochondrial membrane potential (Δψ) and morphology are considered key readouts of mitochondrial functional state. This morphofunction can be studied using fluorescent dyes ("probes") like tetramethylrhodamine methyl ester (TMRM) and Mitotrackers (MTs). Although these dyes are broadly used, information comparing their performance in mitochondrial morphology quantification and Δψ-sensitivity in the same cell model is still scarce. Here we applied epifluorescence microscopy of primary human skin fibroblasts to evaluate TMRM, Mitotracker Red CMXros (CMXros), Mitotracker Red CMH_2Xros (CMH2Xros), Mitotracker Green FM (MG) and Mitotracker Deep Red FM (MDR). All probes were suited for automated quantification of mitochondrial morphology parameters when Δψ was normal, although they did not deliver quantitatively identical results. The mitochondrial localization of TMRM and MTs was differentially sensitive to carbonyl cyanide-4-phenylhydrazone (FCCP)-induced Δψ depolarization, decreasing in the order: TMRM ≫ CHM2Xros = CMXros = MDR > MG. To study the effect of reversible Δψ changes, the impact of photo-induced Δψ "flickering" was studied in cells co-stained with TMRM and MG. During a flickering event, individual mitochondria displayed subsequent TMRM release and uptake, whereas this phenomenon was not observed for MG. Spatiotemporal and computational analysis of the flickering event provided evidence that TMRM redistributes between adjacent mitochondria by a mechanism dependent on Δψ and TMRM concentration. In summary, this study demonstrates that: (1) TMRM and MTs are suited for automated mitochondrial morphology quantification, (2) numerical data obtained with different probes is not identical, and (3) all probes are sensitive to FCCP-induced Δψ depolarization, with TMRM and MG displaying the highest and lowest sensitivity, respectively. We conclude that TMRM is better suited for integrated analysis of Δψ and mitochondrial morphology than the tested MTs under conditions that Δψ is not substantially depolarized.

1. Introduction

Mitochondria are key suppliers of cellular energy in the form of adenosine triphosphate (ATP). Maintaining this supply requires the integrated activity of the electron transport chain (ETC) and F_oF_1-ATPase, which together constitute the oxidative phosphorylation system

Abbreviations: Δψ, mitochondrial membrane potential; ΔV, plasma membrane potential; *Am*, mitochondrial area; *AR*, mitochondrial aspect ratio; BIN, binary image; CM, chloromethyl; CMXros, Mitotracker Red CMXRos; CMH2Xros, Mitotracker Red CMH_2Xros; COR, background-corrected image; *Dm*, fluorescence intensity; ETC, electron transport chain; *F*, mitochondrial formfactor; FCCP, carbonyl cyanide-4-phenylhydrazone; FOV, field of view; MDR, Mitotracker Deep Red FM; MIM, mitochondrial inner membrane; MG, Mitotracker Green FM; *Mm*, mitochondrial mass; MT, Mitotracker; *Nc*, number of mitochondrial objects per cell; NDF, neutral density filter; PM, plasma membrane; R123, rhodamine 123; ROI, region of interest; TMRM, tetramethylrhodamine methyl ester.

* Corresponding author at: Department of Pediatrics, Amalia Children's Hospital, Radboud Center for Mitochondrial Medicine (RCMM), Radboud University Medical Centre (Radboudumc), P.O. Box 9101, 6500 HB Nijmegen, the Netherlands.
E-mail address: Werner.Koopman@radboudumc.nl (W.J.H. Koopman).

[1] Shared first authors.

https://doi.org/10.1016/j.bbabio.2023.149027
Received 2 May 2023; Received in revised form 30 October 2023; Accepted 4 December 2023
Available online 17 December 2023
0005-2728/© 2023 The Authors. Published by Elsevier B.V. This is an open access article under the CC BY license (http://creativecommons.org/licenses/by/4.0/).

(OXPHOS; [1]). Protons (H^+) are expelled across the mitochondrial inner membrane (MIM) by the ETC, thereby generating an inward-directed trans-MIM proton-motive force (PMF), consisting of an electrical (Δψ; more negative inside) and chemical (ΔpH; more alkaline inside) component [2]. The F_oF_1-ATPase allows the controlled re-entry of protons into the matrix to catalyse the formation of ATP from adenosine diphosphate (ADP) and inorganic phosphate [3,4]. Since ΔpH only contributes ~15 % to the total PMF, the magnitude of the latter is dominated by Δψ [5,6], rendering this potential difference a key parameter of mitochondrial activity [7]. Changes in Δψ are often paralleled by alterations in mitochondrial morphology and *vice versa* [8–15]. In this respect, various chemical fluorescent reporter molecules have been described for specific mitochondrial labelling and/or quantitative Δψ analysis (reviewed in: [16,17]). These fluorescent dyes are used to analyze cell populations and/or isolated mitochondria (*e.g.* using flowcytometry, cuvette or plate reader measurements) or applied to

Table 1
Mitochondrial dyes: structure, staining principle and spectral properties.

Abbreviation	Full name	Molecular structure	Staining principle	Excitation/ emission maxima	Refs
TMRM	TMRM	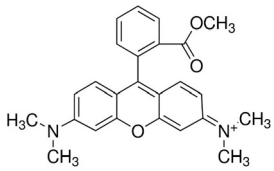	Cell permeant fluorescent cation. Displays Nernstian distribution according to Δψ and ΔV.	552/578 nm	[34] [20] [37] [31]
CMXros	Mitotracker Red CMXros	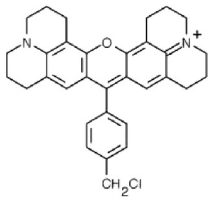	Cell permeant fluorescent cation. Displays Nernstian distribution according to Δψ and ΔV. Contains thiol-reactive chloromethyl group.	579/599 nm	[45] [46] [47] [48] [37] [16]
CMH2Xros	Mitotracker Red CMH_2Xros	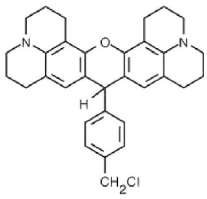	Cell permeant. Derived from dihydro-X-rosamine. Non-fluorescent reduced form of CMXros. Oxidized in the cell to form cationic CMXros. Contains thiol-reactive chloromethyl group.	579/599 nm	[46] [16]
MG	Mitotracker Green FM	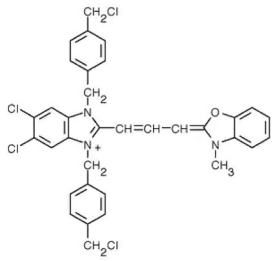	Cell permeant cation. Non-fluorescent in aqueous solution. Becomes fluorescent once accumulated in the lipid environment of mitochondria. Contains thiol-reactive chloromethyl groups. Accumulates in mitochondria regardless of Δψ in certain cell types.	490/512 nm	[46] [48] [37] [16]
MDR	Mitotracker Deep Red FM	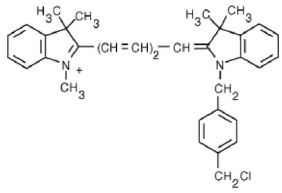	Cell permeant cation. Contains thiol-reactive chloromethyl group.	644/665 nm	[16]

TMRM molecular structure was taken from: www.sigmaaldrich.com, all other molecular structures were taken from: www.thermofisher.com.
Abbreviations: Δψ, mitochondrial membrane potential; ΔV, plasma membrane potential.

visualize mitochondria within single living cells using fluorescence microscopy techniques [18–25].

Using primary human skin fibroblasts (PHSFs), we previously presented strategies for integrated analysis of Δψ and mitochondrial morphology parameters by live-cell fluorescence microscopy and image processing/quantification (*e.g.* [22,26–33]). PHSFs are well suited for such analyses given their relatively large size and flat morphology [30]. Our approach primarily involves the use of fluorescent cations like rhodamine 123 (R123) or tetramethylrhodamine methyl ester (TMRM), which accumulate in the mitochondrial matrix [25,34–38]. Another widely used cation is 5,5,6,6′-tetrachloro-1,1′,3,3′ tetraethylbenzimidazoylcarbocyanine iodide (JC-1), but this fluorescent molecule apparently displays a substantial pH sensitivity [39]. The extent of cation matrix accumulation is Δψ-dependent [40] and described by the Nernst equation:

$$\Delta\psi\ (mV) = -\frac{2.303 \cdot RT}{zF} log_{10}\left(\frac{C_m}{C_{cyt}}\right) \quad \text{(I)}$$

where R is the ideal gas constant (8.3145 $J \cdot K^{-1} \cdot mol^{-1}$), T is the absolute temperature (in K), *z* is the charge of the cation, F is Faraday's constant (96,485 $C \cdot mol^{-1}$), C_m is the mitochondrial matrix concentration of the cation and C_{cyt} is the cytosolic concentration of the cation. In addition, C_m depends on the electrical potential (ΔV; in mV) across the plasma membrane of the cell

$$C_m = C_{ext} \cdot e^{-\frac{(\Delta V + \Delta\psi) \cdot zF}{RT}} \quad \text{(II)}$$

With C_{ext} being the extracellular concentration of the cation [7,31,38,41]. This means that a more negative ΔV (at constant C_{ext} and Δψ), will lead to increased cation accumulation in the mitochondrial matrix, erroneously suggesting that Δψ is more negative (hyperpolarized). Therefore, whenever changes in ΔV are expected, Δψ quantification should be accompanied by control experiments ruling out such changes [42], for instance by electrophysiological analysis [43]. In Eq. (I), the factor before the logarithmic term for mono-cations equals 61 mV at 37 °C. Assuming that Δψ equals ~120–180 mV *in vivo* [27,44], this means that lipophilic mono-cations accumulate between 100- and 1000-fold in the mitochondrial matrix [38].

In addition to R123 and TMRM, also Mitotracker (MT) dyes have been applied for (Δψ-sensitive) mitochondrial staining (Table 1) and (visual) analyses of mitochondrial morphology parameters and mass [8,48–56]. Popular members of the MT family include: Mitotracker Red CMXros (CMXros), Mitotracker Red CMH2Xros (CMH2Xros), Mitotracker Green FM (MG) and Mitotracker Deep Red FM (MDR). CMXros, MG and MDR are cell permeant fluorescent cations, whereas CMH2Xros is cell permeant, non-fluorescent and uncharged. However, upon oxidation CMH2Xros is converted into fluorescent cationic CMXros [45]. Given their cationic nature it is to be expected that mitochondrial fluorescence signals in cells stained with CMXros, CMH2Xros, MG or MDR are ΔV/Δψ-sensitive. These MTs also contain (a different number of) chloromethyl (CM) groups, which can react with accessible nucleophiles (*e.g.* thiol groups of peptides and proteins), thereby potentially forming an aldehyde-fixable conjugate [45,57]. Formation of such conjugates inside the mitochondrial matrix would lead to (partial) MT immobilization, thereby reducing the impact of Δψ depolarization on the MT mitochondrial fluorescence [27,45,48,58–61]. Taken together, it is obvious that proper interpretation of microscopy data obtained with TMRM and/or MT-stained cells requires a side-by-side comparison of these probes. Using the same PHSF cell line (#5120), we here evaluated TMRM and four widely used MT dyes with respect to their performance in automated mitochondrial morphology quantification and sensitivity to Δψ depolarization. We conclude that TMRM is best suited for integrated analysis of Δψ and mitochondrial morphology under conditions when Δψ is not substantially depolarized.

2. Materials and methods

2.1. Cell culture

Primary human skin fibroblasts (PHSFs) were obtained from a healthy individual (#5120) according to the relevant Institutional Review Boards (Radboudumc) and cultured in Medium 199 (M199; Invitrogen Life Technologies, Breda, The Netherlands). This medium was supplemented with 10 % (v/v) fetal bovine serum (Invitrogen) and 100 IU/ml penicillin/streptomycin (Invitrogen). Cells were grown at 37 °C (95 % air, 5 % CO_2) until ~70 % confluence.

2.2. Time lapse fluorescence microscopy of TMRM and Mitotracker dyes

PHSFs were seeded at a density of 10,000/dish (WillCo Dishes; HBST-3522; WillCo Wells B.V., Amsterdam, The Netherlands) and cultured in M199 (37 °C in 95 % air, 5 % CO_2). Following 4 days of culturing, cells were stained for 25 min in M199, containing 15 nM tetramethylrhodamine methyl ester (TMRM; T668; Thermo-Fisher Scientific, Landsmeer, The Netherlands). Under these conditions, TMRM operated in non-quenching/redistribution mode [62,63]. This means that the concentration of TMRM in the mitochondrial matrix is sufficiently low to prevent auto-quenching of its fluorescence signal. More details on the relevance of quenching-related phenomena in mitochondrial morphofunctional analyses are provided elsewhere [64]. For the Mitotrackers (MTs) identical staining conditions were applied with the following concentrations: 50 nM Mitotracker Red CMXros (CMXros; M7512; Thermo-Fisher), 50 nM Mitotracker Red CMH_2Xros (CMH2Xros; M7513; Thermo-Fisher), 50 nM Mitotracker Green FM (MG; M7514; Thermo-Fisher) or 50 nM Mitotracker Deep Red FM (MDR; M22426; Thermo-Fisher). The used MT concentrations and incubation times were according to the manufacturer's instructions and compatible with other experimental studies (*e.g.* [21,48,61,65,66]). Stock solutions of TMRM, MTs and FCCP were freshly prepared in dimethyl sulfoxide (DMSO; #D5879, Sigma), and diluted at least 1000-fold to reach the indicated concentrations. Next, cells were washed twice with PBS, placed in 500 μl of HEPES-Tris (HT) solution (pH 7.4; 132 mM NaCl; 4.2 mM KCl; 1 mM $CaCl_2$; 1 mM $MgCl_2$; 5.5 mM D-glucose; 10 mM HEPES), and mounted in a temperature-controlled chamber (37 °C; ibidi GmbH, Gräfelfing, Germany) attached to the stage of an inverted microscope (Zeiss Axio Observer 7; Carl Zeiss, Jena, Germany) equipped with a Sutter Lambda DG-5 light source (Sutter Instrument, Novato, CA, USA). Under these conditions (*i.e.* in the absence of extracellular TMRM), we previously demonstrated in the same cell line that the mitochondrial TMRM signal was stable for at least 15 min after staining [27]. This strongly suggests that cellular and/or mitochondrial extrusion and leakage are absent during this time period, arguing against active TMRM extrusion by multi drug resistance transporters. To induce depolarization of the mitochondrial membrane potential (Δψ) the mitochondrial uncoupler carbonyl cyanide-4-phenylhydrazone (FCCP; C2920; Sigma-Aldrich) was added to the cells by gentle pipetting. FCCP was applied at a concentration of 15 μM in HT solution (500 μl), which was 2-fold diluted upon addition to the cells. This assured rapid mixing yielding a final FCCP concentration of 7.5 μM (compatible with previous studies; [45,58–61,66]). Fluorescence images were acquired using a Fluar 40×/1.30 Oil M27 objective (Carl Zeiss), appropriate combinations of excitation/emission filters and dichroics (Supplementary Table S1) and a Zeiss Axiocam 702 CCD camera (Carl Zeiss). Time lapse recordings were performed by acquiring 16-bit fluorescence images (1920 × 1216 pixels; 6.8259 pixels/μm) using an acquisition interval of 20 s and various neutral-density filter (NDF) and image exposure settings (Supplementary Table S1). Image sequences were stored in CZI format (16-bit) and intensities in selected regions of interest (ROI) were quantified over time using FIJI software (https://imagej.net/Fiji; version 1.53c). ROIs (Fig. 1A) were positioned in a mitochondria-dense region ("m") and another in the nucleoplasm ("n") of each individual cell. In this way,

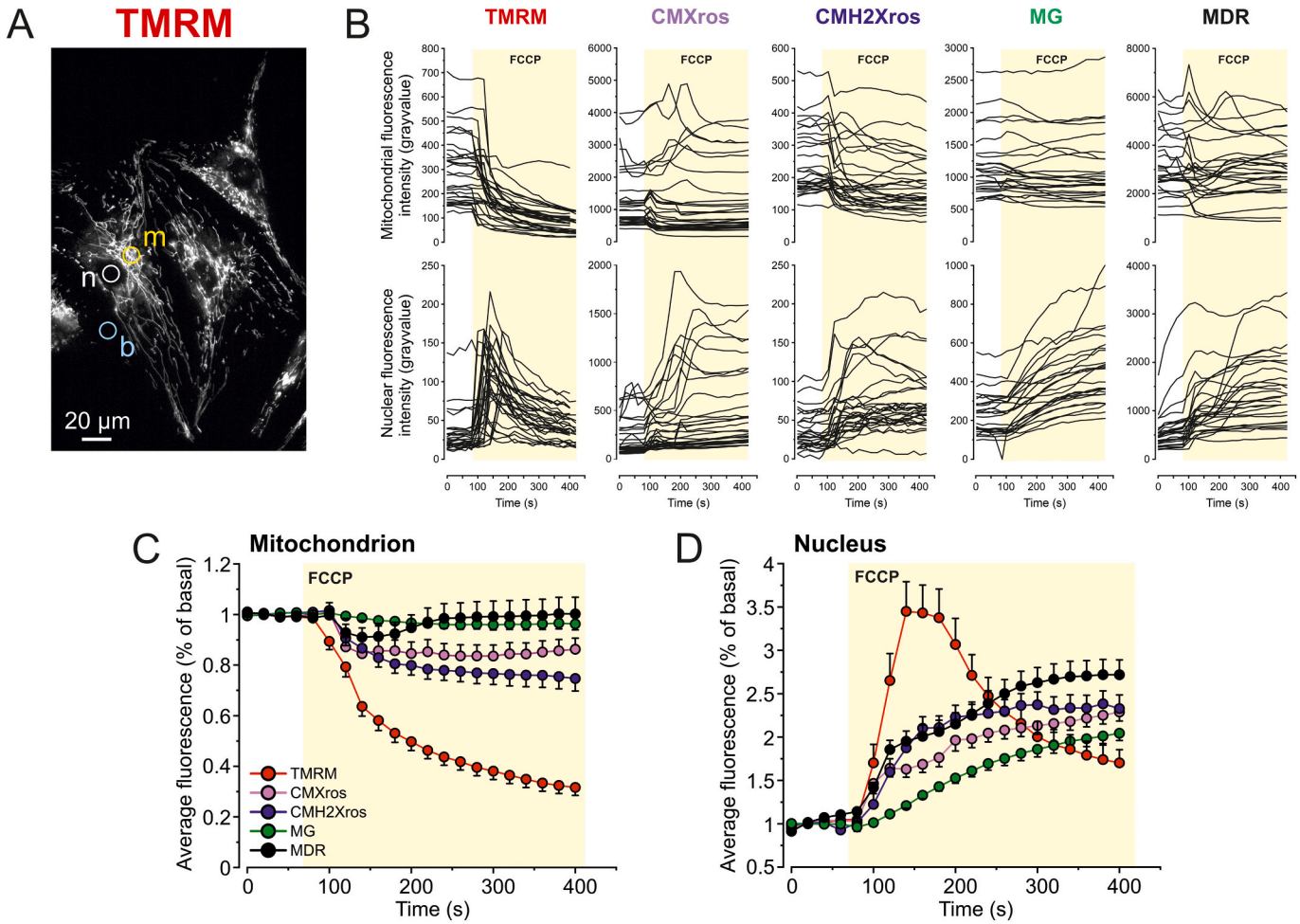

Fig. 1. Time-dependent effect of FCCP on the mitochondrial and nuclear fluorescence intensity of TMRM and Mitotracker dyes. Primary human skin fibroblasts (PHSFs) were stained with TMRM or various Mitotracker dyes (CMXros, CMH2XRos, MG, MDR; Table 1). Fluorescence images were recorded using an interval of 20 s and the mitochondrial uncoupler FCCP (7.5 μM) was added to induce Δψ depolarization. (A) 1st image (RAW) of the timelapse recording visualizing the fluorescence signals in the absence of FCCP. For intensity analysis, background-corrected fluorescence signals were quantified for each cell using ROIs placed in a mitochondria-dense region (marked "m"), a nuclear region ("n") and a closely juxtaposed extracellular background region ("b"). (B) Effect of FCCP on mitochondrial (upper row) and nuclear (lower row) fluorescence signals. (C) Average mitochondrial fluorescence signals computed from the data in panel B (upper row). Prior to calculating this average, for each cell recording the fluorescence intensity data was normalized using the average of the first three datapoints of the image sequence. (D) Same as panel C, but depicting the average nuclear fluorescence signals calculated from the data in panel B (lower row). Statistics: the data in this figure was obtained from at least 25 cells for each condition in 3 independent experiments (days; Table 2). In panel B, each line represents an individual cell. The error bars in panel C and D reflect the standard error of the mean (SEM). (For interpretation of colors used in this figure, the reader is referred to the web version of this article.)

mitochondrial dye release is reflected by a fluorescence decrease and increase in the mitochondrial and nucleoplasmic ROI, respectively. Both signals were background-corrected by subtracting the fluorescence signal in a close-by extracellular ROI ("b").

2.3. Automated quantification of mitochondrial morphology and fluorescence intensity parameters

Images in CZI format were opened by drag-and-drop in FIJI software (version 1.51n), combined into a stack, and saved in TIFF format. TIFF image stacks were opened in Image Pro Plus software (Media Cybernetics, Rockville, MD, USA) and mitochondrial fluorescence intensity and morphology parameters were obtained by image segmentation and quantification. In brief, 16-bit images (RAW) were background-corrected by subtracting the extracellular (background) intensity (gray value), determined using an extracellular region of interest (ROI). This yielded background-corrected 16-bit "COR" images. The latter were converted to 8-bit images using best-fit rescaling (yielding 8-bit "COR" images). The 8-bit COR images were subsequently processed by applying a linear contrast stretch (LCS) operation, top-hat filtering (THF) a median filter (MED) and a thresholding (T) operation using a gray value of 128. This yielded binary (BIN) images highlighting mitochondrial objects (white) on a black background. The latter images were quantified to obtain the area of the individual fluorescent objects (A_m; in pixels), the number of objects per cell (*Nc*), the aspect ratio of the objects (*AR*; being the ratio between the major and minor axis of the ellipse equivalent to the object) and the formfactor (*F*; a.k.a. "roundness", a combined measure of mitochondrial length and degree of branching, $F = \text{Perimeter}^2/4\cdot\pi\cdot\text{Area}$) of the objects. Lower and higher values of *AR* and *F*, correspond to more circular and more elongated/branched morphologies, respectively. Given their extremely flat morphology [30] the product of *Am* and *Nc* can be used as a measure of mitochondrial mass (*Mm*). To analyze the fluorescence intensity of individual objects (*Dm*; grayvalue), 8-bit BIN images were used to mask the 16-bit COR images to yield "masked" (MSK) images. To reduce the influence of noise pixels, only objects with an *Am* value >10 pixels were included in the analysis. The above approach was described in detail and applied/validated using PHSFs previously (*e.g.* [22,26–33]).

2.4. Time lapse fluorescence microscopy of photo-induced mitochondrial Δψ flickering in cells co-stained with TMRM and MG

Prior to microscopy analysis, fibroblasts were seeded at a density of 100,000 cells on glass coverslips (Ø 24 mm; placed in 6 well-plates) and cultured in M199 to ~70 % confluence in a humidified atmosphere (95 % air, 5 % CO_2, 37 °C) during 24 h. Next, cells were stained in M199 (37 °C in 95 % air, 5 % CO_2, 25 min) containing 15 nM TMRM and 50 nM MG. Then, cells were washed 2 times with PBS and coverslips were mounted in a temperature-controlled chamber attached to the stage of an inverted microscope (Axiovert 200 M; Carl Zeiss) equipped with a ×63/1.25 Oil Plan NeoFluar objective [67]. During image acquisition, cells were placed in M199. TMRM was excited at 540 nm using a Xenon lamp-based monochromator with a spectral bandwidth of 15 nm (Polychrome IV; TILL Photonics, Gräfelfing, Germany). MG was excited at 488 nm. A CoolSNAP HQ monochrome CCD-camera (Roper Scientific Photometrics, Vianen, The Netherlands) was used for fluorescence detection. Further details of the spectral properties of this microscopy system (dichroic mirrors, emission filters), as well as image acquisition settings, are provided in Fig. 5A–D and Supplementary Table S1. Microscopy hardware was controlled using Metafluor 6.0 software (Universal Imaging Corporation, Downingtown, PA, USA). To visualize Δψ flickering, individually acquired time-lapse images were combined into a single sequence (stack) using Image Pro Plus software (Media Cybernetics). Next, a "difference" (Δ) sequence was calculated by subtracting the (n-1)th image from the nth image. This movie was optimized using a linear contrast stretch (LCS) operation to visualize decreases and increases in fluorescence signal (*i.e.* occurring between two subsequent images) as black and white pixels, respectively [49,62,68]. During some recordings the cells required manual refocusing. This induced a simultaneous signal change in the Δ image (*e.g.* Supplementary Movie S7). Images with refocusing-induced artifacts were omitted from the analysis [49].

2.5. Minimal model for TMRM redistribution during a single Δψ flickering event

To simulate the inter-mitochondrial exchange of TMRM during reversible Δψ depolarization, a minimal mass action-based model was developed (Supplementary Fig. S3). This model was implemented in MATLAB/Simulink (Release 2022a; www.mathworks.com). Further details are provided in the Results section.

2.6. Data analysis

Analyses were performed with Origin Pro software (Originlab Corp., Northampton, MA, USA). For linear curve fitting, Pearson's correlation coefficient R was used as an estimate of the population correlation coefficient. Values of −1 and +1 indicate a perfect linear relationship between the two variables [69]. Unless stated otherwise, average data was expressed as mean ± SEM (standard error of the mean), differences between conditions were assessed using a non-parametric Mann-Whitney *U* test, and significance was marked as: $^{*}p < 0.05$, $^{**}p < 0.01$ and $^{***}p < 0.001$.

3. Results

3.1. Effect of FCCP on the mitochondrial and nuclear fluorescence intensity of TMRM and MT dyes

Primary human skin fibroblasts (PHSFs) were stained with various mitochondrial dyes (Table 1): tetramethylrhodamine methyl ester (TMRM), Mitotracker Red CMXros (CMXros), Mitotracker Red CMH2Xros (CMH2Xros), Mitotracker Deep Red FM (MDR) or Mitotracker Green FM (MG). To determine how Δψ depolarization affected the mitochondrial fluorescence signals of these dyes, cells were acutely treated with the protonophore carbonyl cyanide-4-phenylhydrazone (FCCP). Since all dyes use a single excitation and single emission wavelength, fluorescence intensity was quantified in a mitochondrial (Fig. 1A; "m") region of interest (ROI) and in the cell nucleus (Fig. 1A; "n") to minimize potential FCCP-induced defocussing artifacts and thereby facilitate data interpretation. FCCP application induced a decrease in mitochondrial fluorescence paralleled by an increase in nuclear signal intensity for all dyes (Fig. 1B). Visual inspection of the average dye responses demonstrated that the magnitude of the fluorescence changes decreased in the order: TMRM ≫ CHM2Xros = CMXros > MDR > MG (Fig. 1C–D). Quantitative single-cell analysis (Table 2) of the data in Fig. 1 demonstrated that the initial (*i.e.* pre-FCCP) mitochondrial ($F_{0,mito}$) and nuclear ($F_{0,nuc}$) staining intensity were spread over a wide range of values and increased in the order: TMRM = CMH2Xros < CMXros = MG < MDR (Fig. 2A-B-C and Table 2). The ratio between mitochondrial and nuclear staining intensity ($F_{0,mito}/F_{0,nuc}$) varied over a much smaller range and increased in the order: MG < CMXros = MDR < CMH2Xros < TMRM (Fig. 2D and Table 2). To assess the magnitude of the FCCP-induced effect, the maximal nuclear fluorescence signal (Nuc%; expressed as percentage of $F_{0,nuc}$) and the minimal mitochondrial fluorescence signal (Mito%; expressed as percentage of $F_{0,mito}$) were determined using the data in Fig. 1B. Nuc% was a linear function of Mit%, revealing that the magnitude of the FCCP effect decreased in the order: TMRM ≫ CMH2Xros = CMXros = MDR > MG (Fig. 2E–F). To determine whether Δψ was necessary for mitochondrial staining, cells were incubated with TMRM or one of the MTs in the presence of FCCP (7.5 μM). Under these conditions the cellular staining patterns were similar to those observed in pre-stained (acutely FCCP-treated), cells (Fig. 3B; "Post-FCCP" condition), and the signal to background ratio increased in the order: TMRM < CMH2Xros = CMXros < MG < MDR (Supplementary Fig. S1A). These results demonstrate that the mitochondrial localization of TMRM, CMXros, CMH2Xros, MG and MDR is differentially sensitive to FCCP-induced Δψ depolarization.

3.2. Effect of FCCP on automated mitochondrial segmentation in cells stained with TMRM or MT dyes

We previously presented an image segmentation protocol for quantification of mitochondrial staining intensity and morphology parameters (see: Materials and methods). This protocol was originally developed for confocal and epifluorescence microscopy analysis of living PHSFs stained with R123 or TMRM. To determine how FCCP-induced Δψ depolarization impacted on the performance of this segmentation algorithm, the first (pre-FCCP) and last (post-FCCP) images of typical timelapse recordings (Fig. 1) were processed (Fig. 3). This yielded a binary (BIN) image highlighting mitochondrial objects (white) on a black background. In the absence of FCCP, the BIN images (Fig. 3A) were suited for computer-assisted quantification of mitochondrial objects. In contrast, the image segmentation algorithm highlighted a large number of relatively small white objects in the BIN images of FCCP-treated cells (Fig. 3B). Comparison of the RAW and BIN/ZOOM images in the post-FCCP situation indicated that these objects do not (exclusively) represent mitochondria. This means that our image quantification protocol is appropriate for analysis of TMRM- and MT-stained PHSFs in the absence, but not in the presence, of FCCP. Quantification of the BIN image yielded various mitochondrial morphology parameters (Table 2), including the area of individual fluorescent objects (A_m), the number of objects per cell (*Nc*), the aspect ratio of the objects (*AR*; being the ratio between the major and minor axis of the ellipse equivalent to the object) and the formfactor (*F*) of the objects. Lower and higher values of *AR* and *F*, correspond to more circular and more elongated/branched morphologies, respectively. Given their extremely flat morphology [30], *Am* can be interpreted as a measure of mitochondrial size, whereas the product of *Am* and *Nc* constitutes a measure of mitochondrial mass (*Mm*). In addition to the morphology

Table 2
Experimental parameters obtained from microscopy experiments.

Dye →	TMRM	CMXros	CMH2Xros	MG	MDR
Initial staining intensities (pre-FCCP)					
n_{cells}	30	31	29	25	27
$F_{0,mito}$ (grayvalue)	299.3 ± 25.74	1291 ± 168.5	246.8 ± 18.91	1171 ± 100.6	3253 ± 248.1
$F_{0,mito}$ (SD%)	47.11	72.69	41.25	43.00	40.63
$F_{0,nuc}$ (grayvalue)	32.26 ± 4.603	233.8 ± 35.66	36.28 ± 4.501	238.5 ± 21.92	587.3 ± 78.55
$F_{0,mito}/F_{0,nuc}$ (A.U.)	11.12 ± 0.9758	6.718 ± 0.4874	9.123 ± 1.203	5.266 ± 0.3574	6.618 ± 0.6010
Effect of FCCP					
Mito%	30.68 ± 3.137	75.06 ± 2.941	67.00 ± 3.264	91.23 ± 1.548	82.50 ± 3.312
Nuc%	430.6 ± 34.05	242.5 ± 10.75	273.2 ± 17.48	204.6 ± 8.400	275.7 ± 17.61
Nuc%/Mito% (A.U.)	17.74 ± 2.093	3.392 ± 0.2079	4.290 ± 0.4185	2.273 ± 0.1149	3.685 ± 0.400
Mitochondrial morphology analysis (pre-FCCP)					
n_{FOV}	7	7	8	7	6
Dm (grayvalue)	242.6 ± 23.51	1059 ± 212.0	189.3 ± 27.54	1017 ± 148.8	2467 ± 310.6
Mm (pixels)	25,001 ± 4234.9	24,369 ± 2351.5	25,079 ± 1530.8	25,021 ± 2433.9	22,976 ± 2809.3
Nc	374.2 ± 65.08	275.7 ± 39.75	384.8 ± 30.99	341.5 ± 48.98	210.1 ± 31.05
Am (pixels)	67.39 ± 4.472	93.29 ± 9.990	67.56 ± 5.330	77.04 ± 5.527	113.0 ± 10.34
AR (A.U.)	3.000 ± 0.09759	3.143 ± 0.1863	2.763 ± 0.0730	3.029 ± 0.1358	3.517 ± 0.1537
F (A.U.)	2.714 ± 0.1455	3.286 ± 0.3481	2.638 ± 0.1463	2.800 ± 0.1512	3.800 ± 0.3088

Data was obtained for multiple fields of view (FOVs; n_{fov}) and cells (n_{cells}) in three independent experiments ($N = 3$ days). Errors indicate standard error of the mean (SEM).
Initial staining intensities (pre-FCCP): Signals were background-corrected for each individual cell. $F_{0,mito}$ = initial mitochondrial fluorescence intensity prior to addition of FCCP (average of first 3 images). SD% = percent standard deviation of $F_{o,mito}$ = relative variation in staining intensity. $F_{0,nuc}$ = initial nuclear fluorescence intensity prior to addition of FCCP (average of first 3 images).
Effect of FCCP: Mito% = Minimal mitochondrial signal (% of $F_{0,mito}$). Nuc% = Maximal nuclear signal (% of $F_{0,nuc}$). ($F_{0,mito}/F_{0,nuc}$) and Nuc%/Mito% were calculated for each individual cell.
Mitochondrial morphology analysis (pre-FCCP): Only objects with a size >10 pixels were included in the analysis. *Dm* = mitochondrial fluorescence intensity; *Nc* = number of stained objects. *Am* = mitochondrial area (a measure of mitochondrial size). *AR* = mitochondrial aspect ratio (a measure of mitochondrial length). *F* = mitochondrial formfactor (a combined measure of mitochondrial length and degree of branching). Mitochondrial mass (*Mm*) is given by the product of *Am* and *Nc*.

parameters, the fluorescence intensity of individual objects (*Dm*) was quantified from "masked" (MSK) images, which were obtained by performing a Boolean "AND" operation using the COR image and its corresponding BIN image [22,31]. The *Dm* values differed between the five dyes (Fig. 4A) and linearly correlated with $F_{0,mito}$ (Supplementary Fig. S1B). The latter demonstrates that manual ($F_{o,mito}$) and automated (*Dm*) quantification of mitochondrial fluorescence intensity delivers similar results. Regarding mitochondrial morphology parameters *Mm* was identical between dyes (Fig. 4B). Moreover, *Nc*, *Am*, *AR* and *F* were similar for TMRM, CMXros, CMH2Xros and MG, but higher for MDR (Fig. 4C-D-E-F). We previously highlighted the importance of (Δψ-linked changes in) mitochondrial staining intensity for proper quantification of *AR* and *F* [29]. In this sense, the linear contrast optimization (LCS) during image processing enhances all signals that are above background, which minimizes the effect of regional differences in Δψ on the outcome of the automated mitochondrial morphology analysis. Therefore the latter will only be affected upon a dramatic loss of Δψ (depolarization), leading to a substantial reduction in mitochondrial fluorescence intensity, as observed in our FCCP experiments (Fig. 3B). Given the relevance of mitochondrial staining intensity in our mitochondrial morphology quantification protocol, we analyzed the relationship between *Dm* and the morphology parameters. This demonstrated both significantly negative (*Mm*, *Nc*) and positive (*Am*, *AR*, *F*) linear correlations (Supplementary Fig. S2). These findings demonstrate that, (1) with the exception of *Mm*, mitochondrial morphology parameters in MDR-stained cells differ from those obtained with the other dyes, and (2) this difference is likely due to the high mitochondrial fluorescence intensity observed for MDR.

3.3. Impact of photo-induced Δψ flickering on the mitochondrial fluorescence signals of TMRM and MG in co-stained cells

Given the highest and lowest sensitivity to FCCP treatment of TMRM and MG, respectively (Figs. 1C–D, 2E), we hypothesized that these dyes should also display the highest (TMRM) and lowest (MG) sensitivity to rapid and reversible Δψ depolarization. It has been previously demonstrated that illumination of mitochondria-localized TMRM or the related tetramethylrhodamine ethyl ester (TMRE) triggers Δψ "flickering", which is characterized by cycles of cation efflux (Δψ depolarization) and influx (Δψ repolarization). This flickering phenomenon reflects reversible opening of the mitochondrial permeability transition pore (mPTP) as demonstrated in a variety of cell models and isolated mitochondria [49,62,68,70–79]. To allow proper analysis, we first compared the spectral properties of TMRM and MG. Using epifluorescence microscopy, PHSFs were stained with either TMRM or MG and visualized (see: Material and methods and Supplementary Table S1). Inspection of the excitation/emission spectra and maxima for TMRM and MG (Fig. 5A) suggests that excitation of MG at 488 nm (Fig. 5B; marked "1") also induces (minor) excitation of TMRM (Fig. 5B; marked "2"). However, excitation of TMRM at 540 nm (Fig. 5B; marked "3") does not excite MG (Fig. 5B; marked "4"). Excitation wavelengths, dichroic mirrors and emission filters were chosen in such a way to minimize the spectral crosstalk between TMRM and MG (Fig. 5C–D and Table S1). Experimental analysis of TMRM-stained cells revealed that mitochondrial TMRM fluorescence signals were not detected in the MG channel (Fig. 5E upper panels, Fig. 5F right panel and Fig. 5G). Similarly, mitochondrial MG fluorescence signals were not detected in the TMRM channel in MG-stained cells (Fig. 5E lower panels, Fig. 5F left panel and Fig. 5H). This demonstrates that our staining protocol and microscopy hardware settings are suited for analysis of TMRM and MG fluorescence signals in co-stained cells. To trigger and visualize photo-induced Δψ flickering in PHSFs we adapted an experimental protocol (Fig. 6A) based upon our previous analyses of mPTP-linked Δψ flickering in mouse myotubes and melanoma cell lines [49,68]. This entailed increasing the intensity of the excitation light by omitting the neutral density filter (NDF) and using a 6-fold (TMRM; 300 ms) longer exposure time relative to the FCCP experiments (Supplementary Table S1). Moreover, the image acquisition interval was reduced to 2 s during Δψ flickering

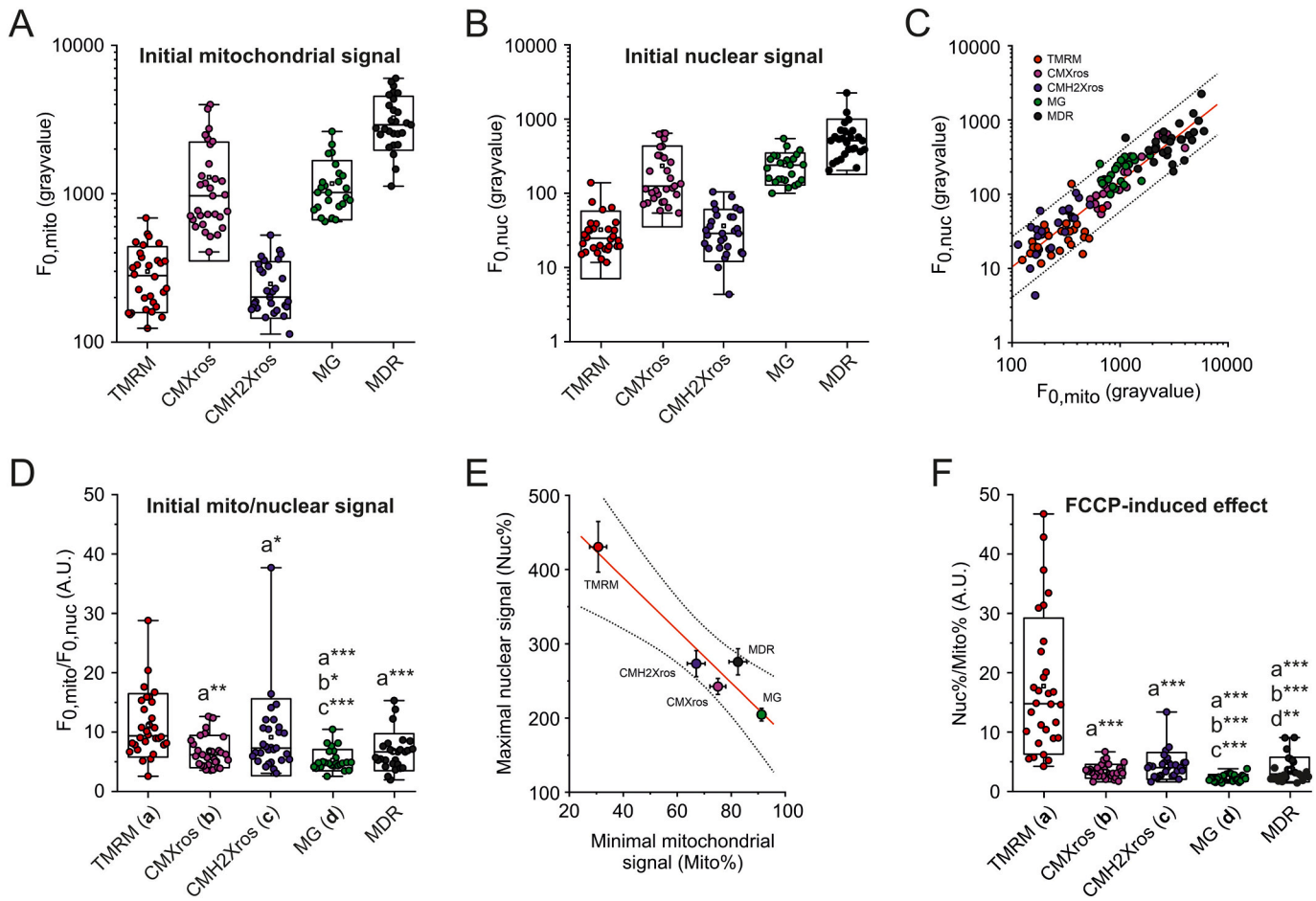

Fig. 2. Quantitative analysis of the mitochondrial and nuclear fluorescence intensity of TMRM and Mitotracker dyes in the absence and presence of FCCP. (A) Background-corrected mitochondrial fluorescence signal ($F_{0,mito}$) computed from the first three images within the image sequence for each cell (Fig. 1B; upper panels). (B) Same as panel A, but now for the background-corrected nuclear fluorescence signal ($F_{0,nuc}$) for each cell (Fig. 1B; lower panels). (C) Scatter plot of the data in panel A ($F_{0,mito}$) *vs.* panel B ($F_{0,nuc}$). The red line indicates a linear fit: $R = 0.935$, $p < 0.0001$, slope = 1.15 ± 0.0370 (SE), intercept = −1.27 ± 0.107(SE). Dotted lines represent the 95 % prediction limits of the fit. (D) Ratio between the mitochondrial and nuclear fluorescence signals ($F_{0,mito}/F_{0,nuc}$) for each cell. (E) Effect of FCCP treatment on average fluorescence signals expressed as the minimal mitochondrial intensity (Mit%; expressed as percentage of $F_{0,mit}$) and the maximal nuclear intensity (Nuc%; expressed as percentage of $F_{0,nuc}$). The red line indicates a linear fit: $R = -0.960$, $p = 0.00983$, slope = −3.54 ± 0.602(SE), intercept = 530 ± 43.6(SE). Dotted lines represent the 95 % confidence limits of the fit. (F) Quantification of the FCCP induced effect as expressed by the ratio Nuc%/Mit %. Statistics: In panel A, B, C, D, and F, each symbol represents an individual cell, error bars mark the 99 % (upper) and 1 % (lower) percentile, the box marks the SD, the square marks the mean value, and the horizontal line within the box indicates the median value. Significant differences between conditions (a, b, c, d) were assessed using a non-parametric Mann-Whitney *U* test and marked by: *p < 0.05, **p < 0.01 and ***p < 0.001. (For interpretation of the references to colour in this figure legend, the reader is referred to the web version of this article.)

experiments. As a consequence, repetitive and reversible Δψ depolarizations are triggered by TMRM-mediated photo-induced stimulation of mitochondrial mPTP opening (*e.g.* [49,62,68]). Microscopy imaging yielded two image sequences for each field of view (FOV), reflecting TMRM and MG time-lapse recordings (Fig. 6B; upper panel and Supplementary Movie S6). To visualize Δψ flickering, a "difference" (Δ) sequence was calculated from each TMRM and MG image sequence (*i.e.* "ΔTMRM" and "ΔMG") by subtracting the (n-1)th image from the nth image (Supplementary Movie S7). In these Δ sequences, decreases and increases in TMRM and MG fluorescence intensity between subsequent images are visualized as regions of black or white pixels, respectively [49,62,68]. This analysis revealed the presence of such decreases/increases in the TMRM sequence but not in the MG sequence (Fig. 6B; lower panel; arrows and Fig. 6C). Manual scoring of the number of depolarizations within discrete image intervals (*i.e.* for images 20 to 70, images 200 to 250 and images 400 to 450) from multiple ΔTMRM sequences demonstrated that the number of Δψ depolarizations per cell increased as a function of time (Fig. 6D). This is compatible with oxidative stress accumulation in the context of the envisioned flickering mechanism, where TMRM illumination stimulates cyclic photogeneration of mitochondrial singlet oxygen molecules ($^1O_2$) that increase mPTP open probability [71,74,80,81]. Taken together, these results support our FCCP results in demonstrating that the mitochondrial localization of TMRM and MG displays a high and low sensitivity, respectively, to reversible Δψ depolarization.

3.4. *Kinetics of a single photo-induced Δψ flickering event in TMRM and MG co-stained cells*

Through serendipity, the depicted experiment displayed a parallel increase in black and white pixels in the ΔTMRM image sequence (Fig. 6C). This provided an opportunity for detailed analysis of mitochondrial TMRM release and uptake kinetics. Between image T708 and T706, TMRM fluorescence decreased in the black mitochondrial filaments and slightly increased in adjacent filaments. Between image T708 and T710, additional TMRM was lost from the mitochondrial filaments (black pixels), whereas adjacent filaments displayed a further increase in TMRM signal (white pixels). Analysis of the TMRM signal (Fig. 7A) using

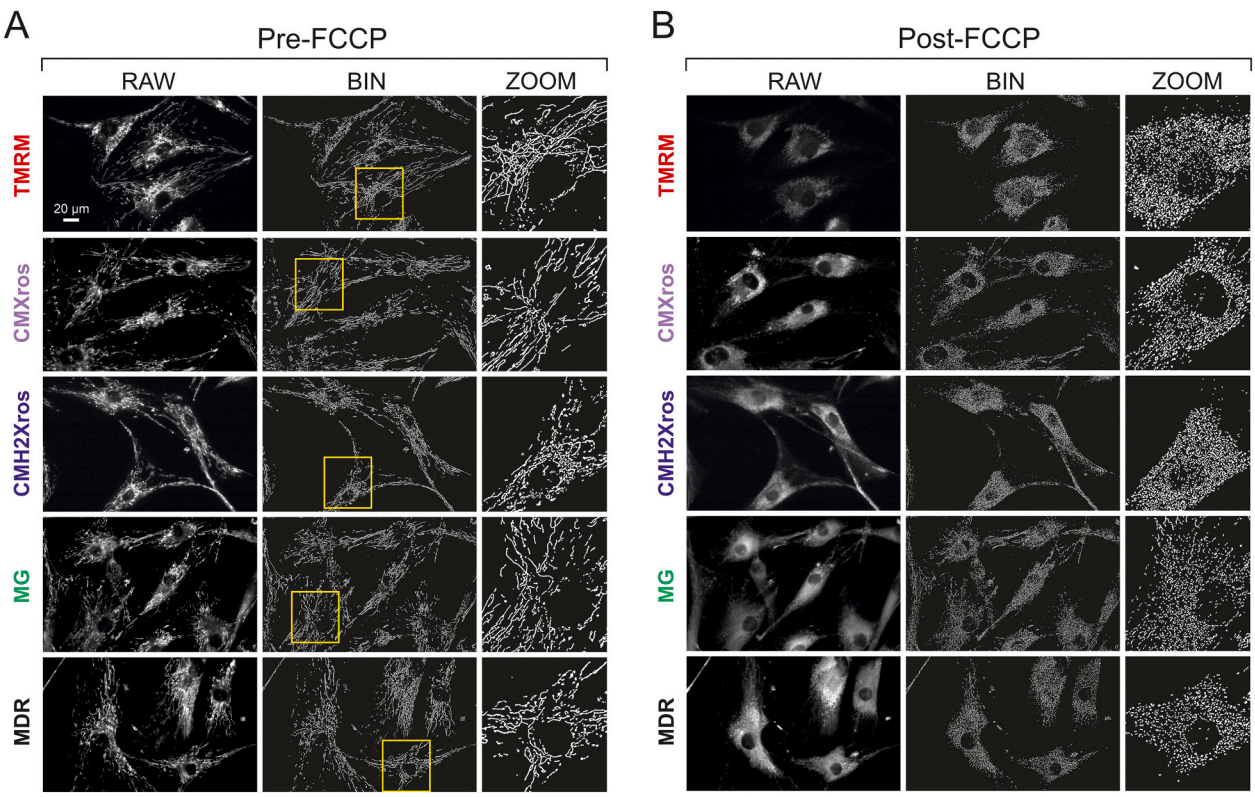

Fig. 3. Effect of FCCP on mitochondrial segmentation in cells stained with TMRM or Mitotracker dyes. The data presented in this figure reflects five typical image sequences (Supplementary Movies S1–S5; representing the experiments in Fig. 1). (A) 1st image (RAW; left column) of the timelapse recording visualizing the fluorescence signals in the absence of FCCP (the top left image is identical to Fig. 1A). Following image segmentation, a binary (BIN) image was obtained (middle column) allowing quantification of mitochondrial morphology parameters. A magnification of the BIN image (yellow square) is presented in the right column (ZOOM), to highlight mitochondrial structures (white objects). (B) Similar to panel A, but now representing the last image of the timelapse recording in the presence of FCCP. Similar to panel A, RAW, BIN and ZOOM images are presented. (For interpretation of the references to colour in this figure legend, the reader is referred to the web version of this article.)

ROIs (Fig. 7B; yellow ovals) positioned on mitochondrial filaments displaying TMRM release (Mito1) and -uptake (Mito2) demonstrated opposite and similar kinetics (Fig. 7C). Only a very minor and transient TMRM fluorescence increase during the depolarization phase of the Δψ flickering event was detected in a closely juxtaposed cytosolic ROI (Fig. 7C; green circles). The Δψ flickering event in Mito 1 had a total duration of ~44 s and consisted of three kinetic phases: a relatively rapid depolarizing phase (phase I; ~8 s), a stationary phase (phase II; ~12 s) and a repolarization phase (phase III; ~24 s). The TMRM fluorescence decrease in Mito1 and increase in Mito2, displayed similar time constants (τ; Fig. 7C). Taken together, these results strongly suggest that TMRM molecules released from a mitochondrial filament undergoing Δψ depolarization (Mito1) are primarily taken up by the nearby mitochondrial filament not undergoing such an event (Mito2). The different phases of the Δψ flickering event suggests that Δψ relatively rapidly depolarizes (phase I) and more slowly recovers (phase III). Given the fact that Δψ is primarily sustained by the ETC [5,6], it is likely that the kinetics of phase II reflects ETC activity (Fig. 7D). To further enhance our understanding of this experimental data, a mass action-based mathematical model was developed to simulate reversible TMRM exchange between Mito1 and Mito2.

3.5. Minimal model for dynamic TMRM redistribution during a reversible Δψ flickering event

Using our experimental data as a starting point (Fig. 7C), we adapted a recently described computational model for reversible Δψ flickering [82]. Our model consisted of two mitochondria (Mito1, Mito2) and a cytosolic compartment (Fig. 8A). It was assumed that TMRM enters the cytosol from Mito1 and Mito2 *via* two outward-directed fluxes ($V_{1,out}$, $V_{2,out}$) and enters Mito1 and Mito2 from the cytosol by two inward-directed fluxes ($V_{1,in}$, $V_{2,in}$):

$$V_{1,out} = [TMRM]_1 \cdot k_{out} \quad \text{(III)}$$

$$V_{2,out} = [TMRM]_2 \cdot k_{out} \quad \text{(IV)}$$

$$V_{1,in} = [TMRM]_c \cdot k_{in} \quad \text{(V)}$$

$$V_{2,in} = [TMRM]_c \cdot k_{in} \quad \text{(VI)}$$

Literature values of k_{out} (the rate constant of TMRM efflux from the mitochondrion) and k_{in} (the rate constant of TMRM influx into the mitochondrion) equalled 0.1 s^{-1} and 0.0002·ABS(Δψ), respectively [82]. These values were obtained from Δψ flickering data in rat ventricular myocytes and smooth muscle cells [80]. Obtaining a good quantitative match with our experimental data required increasing the rate constants to $k_{out} = 0.8\ s^{-1}$ and $k_{in} = 0.2 \cdot ABS(\Delta\psi)$. This suggests that PHSFs display a relatively fast mitochondrial TMRM release and Δψ-dependent TMRM uptake in our experiments. Changes in TMRM concentration ([TMRM]) for Mito1, Mito2 and the cytosol were described using ordinary differential equations (ODEs):

$$\frac{d[TMRM]_1}{dt} = V_{1,in} - V_{1,out} \quad \text{(VII)}$$

$$\frac{d[TMRM]_2}{dt} = V_{2,in} - V_{2,out} \quad \text{(VIII)}$$

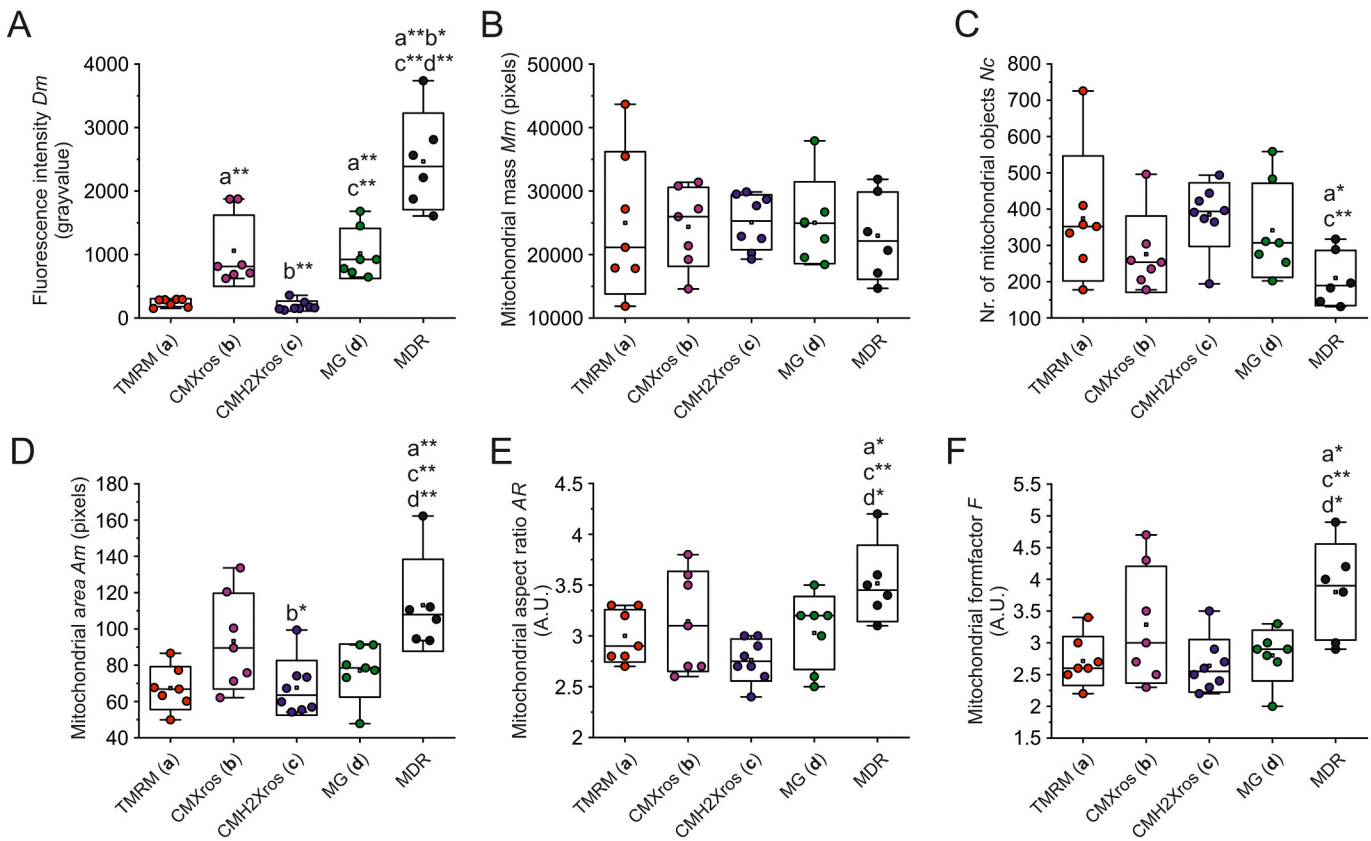

Fig. 4. Quantitative analysis of mitochondrial morphology parameters in cells stained with TMRM or Mitotracker dyes in the absence of FCCP. Mitochondrial morphology parameters were quantified by image segmentation of the 1st image from the timelapse recordings presented in Fig. 1B. (A) Background-corrected mitochondrial fluorescence intensity (*Dm*) for TMRM and the Mitotracker dyes. (B) Same as panel A, but now for mitochondrial mass (*Mm*). (C) Same as panel A, but now for the number of mitochondrial objects per cell (*Nc*). (D) Same as panel A, but now for mitochondrial area (*Am*; a measure of mitochondrial size). (E) Same a panel A, but now for mitochondrial aspect ratio (*AR*). (F) Same as panel A, but now for mitochondrial formfactor (*F*). Statistics: In this figure, each symbol represents a full FOV (microscopy image). Error bars mark the 99 % (upper) and 1 % (lower) percentile, the box marks the SD, the square marks the mean value, and the horizontal line within the box indicates the median value. Significant differences between conditions (a, b, c, d) were assessed using a non-parametric Mann-Whitney U test and marked by: $^{*}p < 0.05$ and $^{**}p < 0.01$.

$$\frac{d[TMRM]_c}{dt} = V_{1,out} - V_{1,in} + V_{2,out} - V_{2,in} \quad \text{(IX)}$$

This model was implemented in MATLAB/Simulink (Supplementary Fig. S3) and its behaviour was investigated using the following assumptions: (1) Mito1 and Mito2 display a resting Δψ of −119 mV, as demonstrated previously in this PHSF cell line [27], (2) the Mito1 flickering event consists of a step-wise Δψ depolarization and repolarization [82], (3) Δψ depolarization occurs instantaneously from −119 mV to 0 mV, (4) the Δψ depolarization has a duration of 20 s, and (5) Δψ instantaneously repolarizes from 0 mV to −119 mV. Using the above Δψ profile for Mito1 (Fig. 8B), the model ("Model A") predicted a rapid reversible loss of TMRM from Mito1 (Fig. 8D; black line), a rapid reversible uptake of TMRM for Mito2 (red line) and a minor change in $[TMRM]_c$ (green line). The predicted duration of phases I and II for Model A agreed well with the experimental data (Fig. 8F; white *vs.* gray bars). In contrast, the duration of phase III predicted by Model A was much shorter than observed in the experiment (Fig. 8F; white *vs.* gray bars), suggesting that the assumed length of the Δψ repolarization phase is too short in this model. Therefore, a second model was developed ("Model B"), which was identical to Model A except for displaying a longer (20 s) Δψ repolarization time (Fig. 8C). The output of Model B (Fig. 8E) agreed well with the duration of phases I, II and III in the experiment (Fig. 8F; white *vs.* black bars). Moreover, the overall TMRM kinetics predicted by Model B matched well with the experimental data (Fig. 8G). Taken together, our modelling results support the conclusion that TMRM redistribution between Mito1, Mito2 and cytosol during a reversible Δψ flickering event is primarily governed by mass action kinetics. In this sense, we propose that phase II of this event is mainly governed by ETC activity.

4. Discussion

This study focuses on the use of TMRM and MT dyes for automated quantification of mitochondrial morphology and Δψ in PHSFs. To allow faithful comparison between dyes and with other studies, all experiments were carried out in the same cell line (#5120) using established staining protocols. It was found that TMRM and MTs are suited for automated mitochondrial morphology quantification, but that the numerical data obtained with different probes is not identical. Moreover, we observed that all probes are sensitive to FCCP-induced Δψ depolarization, with TMRM and MG displaying the highest and lowest sensitivity, respectively. We conclude that TMRM is best suited for integrated analysis of Δψ and mitochondrial morphology than the tested MTs under conditions that Δψ is not substantially depolarized.

4.1. Mitochondrial specificity and FCCP-sensitivity of TMRM and MTs

Under our experimental conditions, all dyes displayed a typical mitochondrial staining pattern (Fig. 3A) and mitochondrial and nuclear fluorescence intensity linearly increased in the order: TMRM = CMH2Xros < CMXros = MG < MDR (Fig. 2C). The ratio between these signals ($F_{o,mito}/F_{o,nuc}$) reflects the degree of mitochondria-

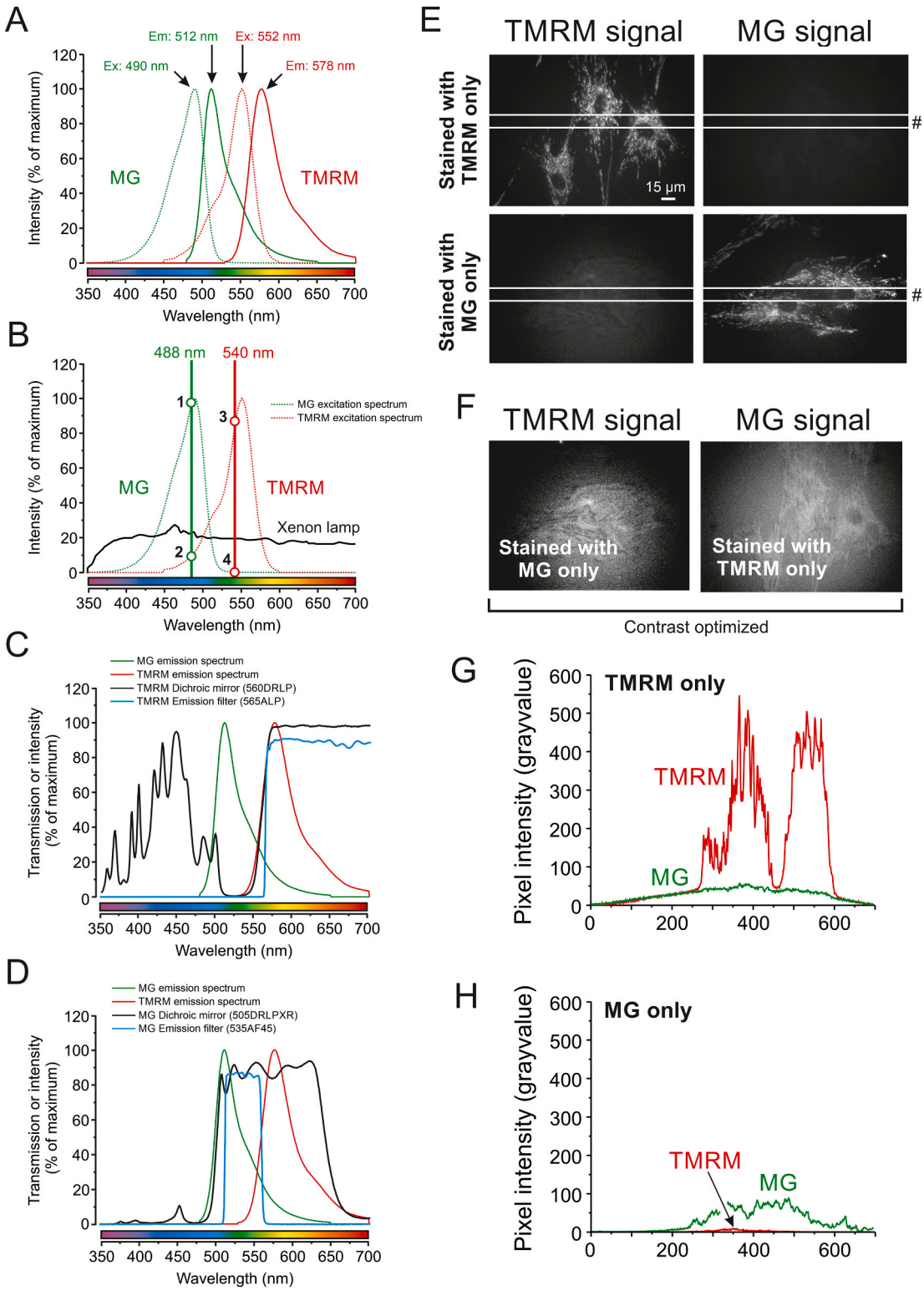

(caption on next page)

Fig. 5. Spectral properties of TMRM and MG. (A) Excitation (Ex; dotted lines) and emission (Em; continuous lines) spectra for TMRM (red) and MG (green). Numerals indicate excitation and emission maxima (nm). (B) Excitation spectra (dotted lines) of TMRM (red) and MG (green). The excitation wavelengths for TMRM (540 nm) and MG (488 nm) used in this study are marked by vertical lines. Excitation of MG (marked "1") does also excite TMRM (marked "2"), whereas excitation of TMRM (marked "3") does not excite MG (marked "4"). The emission spectrum of the used excitation source (Xenon lamp) is depicted by the black curve. (C) TMRM (red) and MG (green) emission spectra, superimposed on the spectral characteristics of the dichroic mirror (560DRLP; black) and emission filter (565ALP; blue line) used for detection of TMRM fluorescence. (D) TMRM (red) and MG (green) emission spectra, superimposed on the spectral characteristics of the dichroic mirror (560DRLPXR; black) and emission filter (535AF45; blue line) used for detection of MG fluorescence. (E) Upper panel: background-corrected fluorescence signals of TMRM-stained cells detected in the TMRM channel (300 ms illumination) and MG channel (100 ms illumination) using the excitation wavelengths, dichroics and emission filters depicted in panels B-C-D. In this panel, a grayvalue display range of 0–1000 (for TMRM and MR) was used for visualization purposes. Bottom panel: same as upper panel, but now for cells stained with MG. Here, a grayvalue display range of 0–200 (for TMRM and MR) was used for visualization. (F) Contrast-optimized versions of the TMRM channel signal in MG-only stained cells (left panel; taken from panel E) and the MG channel signal in TMRM-only stained cells (right panel: taken from panel E). (G) Average intensity for the profile indicated by the horizontal line in panel E (upper panel: for cells stained with TMRM only). (H) Average intensity for the profile indicated by the horizontal line in panel E (lower panel: for cells stained with MG only). Further details are provided in the Results section and Supplementary Table S1. (For interpretation of the references to colour in this figure legend, the reader is referred to the web version of this article.)

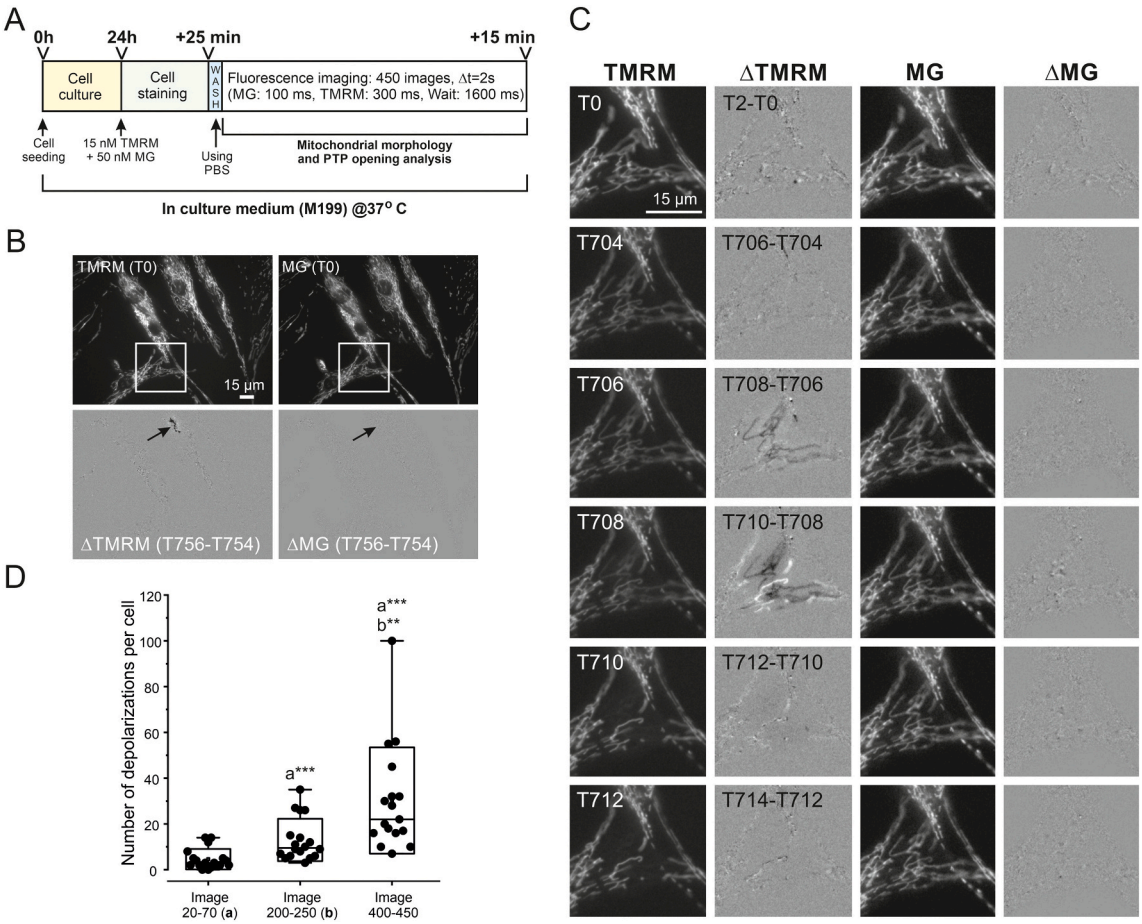

Fig. 6. Impact of photo-induced Δψ flickering on the mitochondrial fluorescence signals of TMRM and MG in co-stained cells. (A) Experimental protocol for cell culture, staining and fluorescence imaging of photo-induced Δψ flickering. (B) Upper panel: TMRM and MG fluorescence signal at the beginning of the image acquisition (T0). This panel depicts background-corrected (COR) images in which gray value display ranges of 0–912 (TMRM) and 0–480 (MG) were used for visualization purposes. The white box highlights the ROI magnified in panel C (for full image sequence see: Supplementary Movie S6). Lower panel: example of difference (Δ) images directly calculated from the time-lapse recording by subtracting COR image T754 (*i.e.* recorded at 754 s) from COR image T756 (*i.e.* the next image recorded at 756 s). The ΔMG and ΔTMRM were contrast-optimized using a linear contrast stretch (LCS) operation for visualization purposes. The dark pixels in the ΔTMRM image reflect the acute loss of TMRM fluorescence from mitochondrial objects (arrow) linked to Δψ depolarization. Such dark pixels were absent from the ΔMG image (for full image sequence see: Supplementary Movie S7). (C) Zoomed-in version of the time-lapse recording in panel B. The columns depict the TMRM fluorescence signal (TMRM), the TMRM difference images (ΔTMRM; for full image sequence see Supplementary Movie S8), the MG fluorescence signal (MG) and the MG difference images (ΔMG). The ΔMG and ΔTMRM images were contrast-optimized using a linear contrast stretch (LCS) operation. (D) Total number of Δψ depolarization events per cell within three discrete image intervals (20–70; 200–250; 400–450). Statistics: the data in panel D was obtained from 18 cells (Image 20–70), 18 cells (Image 200–250) and 17 cells (Image 400–450) in 4 independent experiments (days). Each symbol represents an individual cell, error bars mark the 99 % (upper) and 1 % (lower) percentile, the box marks the SD, the square marks the mean value, and the horizontal line within the box indicates the median value. Significant differences between conditions (a,b) were assessed using a non-parametric Mann-Whitney *U* test and marked as: $^{**}p < 0.01$ and $^{***}p < 0.001$.

specific staining (Fig. 2D and Table 2), which decreased in the order: TMRM > CMH2Xros > MDR = CMXros = MG. This indicates that TMRM staining delivers the most mitochondria-specific signals.

Collectively, the cellular localization of CMXros, MG and MDR depends on (extracellular) probe concentration and their relative rates of PM/MIM transfer and immobilization (Fig. 9). This means that, in

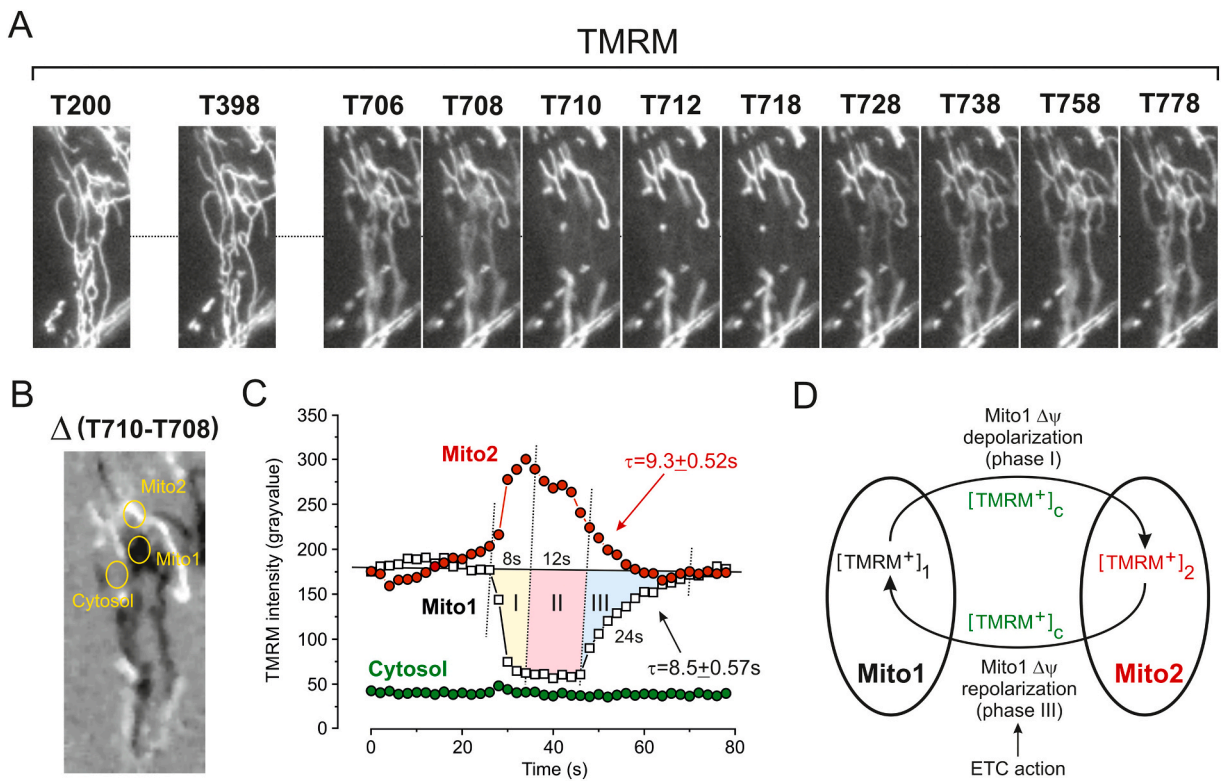

Fig. 7. Kinetics of a single photo-induced Δψ depolarization/repolarisation event in TMRM and MG co-stained cells. (A) Selected images (zoomed-in, rotated and contrast-optimized) visualizing mitochondrial TMRM release and reuptake during the flickering event in Fig. 6C. The full image sequence is provided in Supplementary Movie S9. (B) TMRM difference image (ΔTMRM; contrast-optimized) highlighting the simultaneous decrease (Mito1; black pixels) and increase (Mito2: white pixels) in TMRM intensity occurring between image T708 and image T710. Three regions of interest (ROIs) are highlighted (yellow circles) representing Mito1, Mito2 and the cytosol. (C) Kinetics of the TMRM fluorescence change in the ROIs for Mito1 (open squares), Mito2 (red circles), and the cytosol (green circles), revealing two dynamic phases (I and III) as well as a stationary phase (II). The increase (Mito1) and decrease (Mito2) in TMRM fluorescence during phase III was fitted using a mono-exponential equation: $y = y_0 + A \cdot e^{-t/\tau}$ to obtain the indicated time-constant τ ($R^2 > 0.98$). (D) Proposed mechanism of TMRM redistribution between Mito1, cytosol and Mito2 during the Δψ flickering event (see Results for details). (For interpretation of the references to colour in this figure legend, the reader is referred to the web version of this article.)

theory, CMXros, MG and MDR could end up at the PM, in the cytosol and/or in the mitochondrial matrix. The relevance of extracellular probe concentration is illustrated by our previous observation in cell line #5120 that using a 100-fold higher CMXros or MG concentration of (*i.e.* 5 μM instead of 50 nM) greatly increased extra-mitochondrial staining levels [28]. Evidence in isolated brain mitochondria suggests that this aspecific staining is linked to fact that μM concentrations (but not nM concentrations) of CMXros and MG reduce mitochondrial state 4 (resting) and uncoupled (maximal) oxygen consumption [48]. Compatible with this explanation, MDR (50 nM) did not affect basal/maximal oxygen consumption rates and ATP production in cancer stem cell models [83]. In this sense, the extra-mitochondrial staining in our previous study [28] might be due to (partial) Δψ-depolarization induced by the relatively high extracellular CMXros and MG concentration.

The mitochondrial matrix concentration (C_m) of the cation TMRM (Fig. 9A), depends on the electrical potential across the PM (ΔV) and MIM (Δψ), as well as its extracellular concentration (Eq. (II)). Given their cationic nature, CMXRos (Fig. 9B), MG (Fig. 9D) and MDR (Fig. 9E) likely behave similar to TMRM regarding their Δψ-dependent accumulation in the mitochondrial matrix. However, in contrast to TMRM, CMXros, MG and MDR are (partially) immobilized through their thiol-reactive CM groups (Fig. 9; green symbols). Indeed, the magnitude of the FCCP effect (Fig. 2E) decreased in the order: TMRM ≫ CHM2Xros = CMXros = MDR > MG, whereas the number of CM groups increased in the same order: TMRM ≪ CMH2Xros = CMXros = MDR < MG (Fig. 9). This strongly suggests that mitochondrial probe immobilization by these groups is directly responsible for the differential FCCP effect.

Of the MTs analyzed, CMH2Xros is a special case since it becomes fluorescent (*i.e.* detectable) upon oxidative conversion into CMXros [16,46]. This suggest that similar results should be obtained in CMH2Xros- and CMXros-stained cells. Oxidation of CMH2Xros can occur at various sites in the cell (Fig. 9C), for instance by extracellular ROS (eROS), cytosolic ROS (cROS), and/or mitochondrial ROS (mROS), after which the formed cationic CMXros is expected to behave as described above. Interestingly, in our experiments the mitochondrial and nuclear fluorescence signals of CMXros were >6-fold higher than those of CMH2Xros (Fig. 2A–B and Table 2). Since the used extracellular concentration and microscopy settings were identical for these MTs (Supplementary Table S1), and their molecular structure is highly similar (Fig. 9), this result strongly suggests that the rate of oxidative conversion of CMH2Xros into CMXros is relatively low in our experiments. This means that the mitochondrial CMXros fluorescence intensity in CMH2Xros-stained cells also depends on ROS levels.

Kinetic analysis demonstrated that FCCP application induced a bi-phasic decrease in mitochondrial TMRM fluorescence (Fig. 1C) and an increase followed by a decrease in nuclear TMRM fluorescence (Fig. 1D). The mitochondrial signal decrease for CMXros and CMH2Xros was kinetically similar to TMRM but of a lesser magnitude. In case of MG, only a small mono-phasic drop in mitochondrial fluorescence was observed, whereas for MDR this drop was transient. With respect to the nucleus, the fluorescence signals of CMXros, CMH2Xros, MG and MDR monotonously increased albeit with apparent bi-phasic kinetics (Fig. 1D). Visual inspection of the TMRM timelapse recordings (*e.g.*

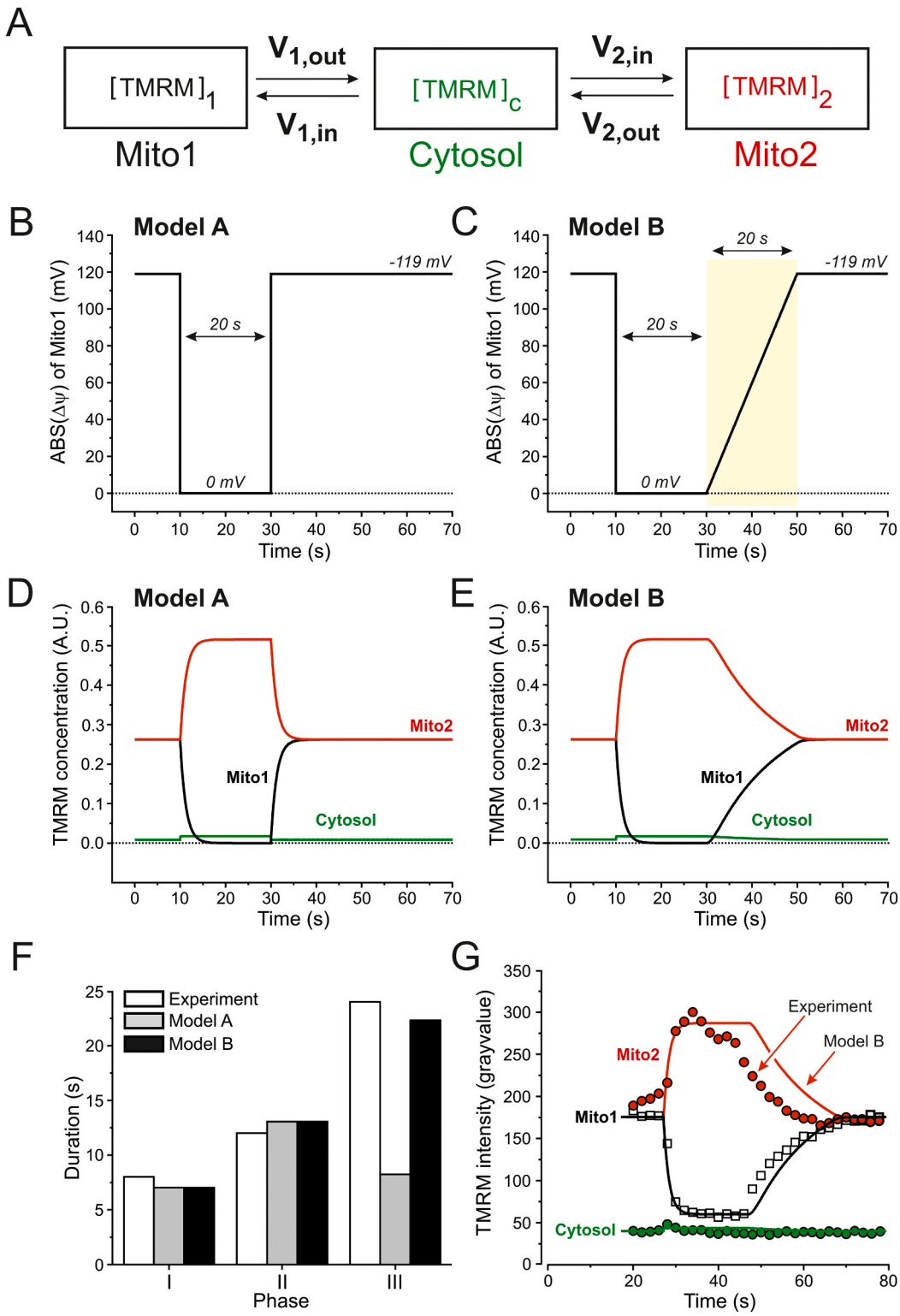

Fig. 8. Minimal model describing the dynamic TMRM redistribution between Mito1 and Mito2 during a reversible Δψ flickering event. (A) Schematic depiction of the three compartments in the model (Mito1, Cytosol, Mito2) and the four exchange fluxes ($V_{1,out}$, $V_{1,in}$, $V_{2,out}$, $V_{2,in}$). The model was applied to simulate the change in TMRM concentration in Mito1 ($[TMRM]_1$), the cytosol ($[TMRM]_c$) and Mito2 ($[TMRM]_2$). Equilibrium analysis yielded the values for the TMRM concentration of 0.2621 ($[TMRM]_1$), 0.2621 ($[TMRM]_2$) and 0.008807 ($[TMRM]_c$). These were used as initial values during simulations. (B) Assumed absolute change in mitochondrial membrane potential (Δψ) of Mito1 during the flickering event (Model A). (C) Similar to panel B but now for a flickering event displaying slower Δψ recovery kinetics (Model B). (D) Predicted [TMRM] kinetics for Mito1 (black line), the cytosol (green line) and Mito2 (red line) during the Δψ flickering event in Model A. (E) Same as panel D but now for Model B. (F) Duration of the dynamic phases (I and III) and stationary phase (II) of the Δψ flickering event in the experiment (open bars; taken from Fig. 7C), Model A (gray bars; phase duration was identical for Mito1 and Mito2), and Model B (gray bars; phase duration was identical for Mito1 and Mito2). (G) Super-positioning of the experimental data (symbols; taken from Fig. 7C) and Model B predictions (lines; taken from Fig. 8E) for Mito1 (open squares), Mito2 (red circles) and the cytosol (green circles). The simulated data was shifted to the right to match the start of the TMRM loss from Mito1. See Results for details. (For interpretation of the references to colour in this figure legend, the reader is referred to the web version of this article.)

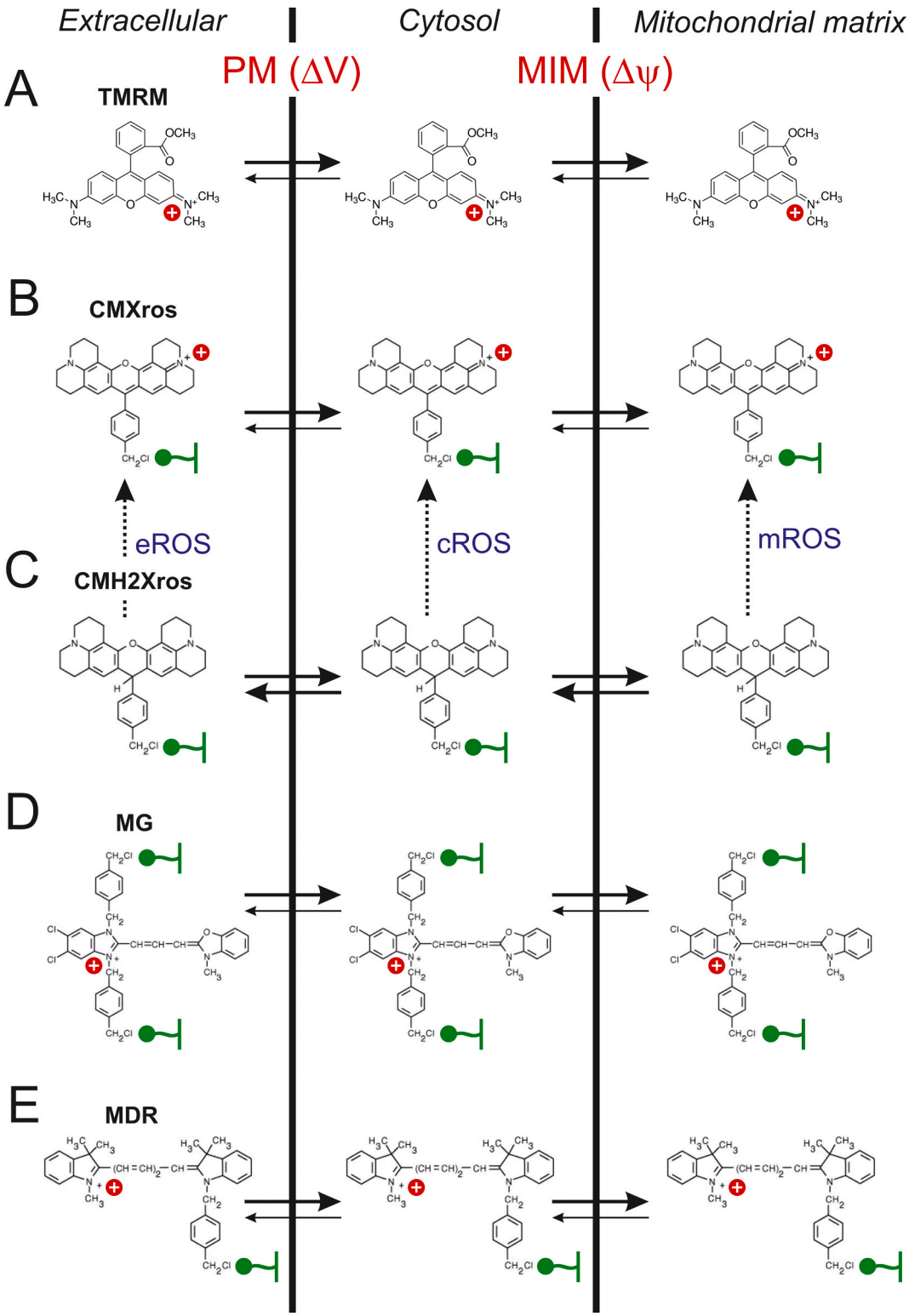

Fig. 9. Mitochondrial staining mechanisms of TMRM and Mitotracker dyes. (A) Mechanism of accumulation of TMRM in the mitochondrial matrix. (B) Same as panel A but now for CMXros. (C) Same as panel A but now for CMH2Xros. (D) Same as panel A but now for MG. (E) Same as panel A but now for MDR. The vertical lines represent the plasma membrane (PM) of the cell and mitochondrial inner membrane (MIM). Molecular movement through these membranes is indicated by arrows, the thickness of which reflects the relative magnitude of the transfer. Positive charges and thiol-reactive chloromethyl groups are indicated by red and green symbols, respectively. Oxidative conversion of CMH2Xros into CMXros can be stimulated by extracellular reactive oxygen species (eROS), cytosolic ROS (cROS) and mitochondrial ROS (mROS). See Discussion for details. (For interpretation of the references to colour in this figure legend, the reader is referred to the web version of this article.)

Supplementary Movie S8) revealed that FCCP treatment subsequently induced: (1) acute TMRM release from elongated mitochondrial filaments, (2) TMRM entry into the nucleus, (3) TMRM exit from the nucleus, and (4) mitochondrial TMRM re-uptake. These phenomena were paralleled by apparent mitochondrial fragmentation (*e.g.* Supplementary Movie S8), as observed previously in human skin fibroblasts and other cell types [9,84]. The fact that the mitochondrial TMRM signal does not return to pre-FCCP levels (Fig. 1C), in combination with the drop in nuclear TMRM signal (Fig. 1D), strongly suggests that post-FCCP Δψ-values are less negative than pre-FCCP Δψ values. This conclusion is strengthened by the observation that TMRM and the MTs displayed a substantial post-FCCP increase in extramitochondrial fluorescence signal (Fig. 3B). Increasing FCCP concentrations (10-30-100-300-1000 nM) dose-dependently stimulated mitochondrial oxygen consumption in isolated rat ventricular myocytes [85]. This is compatible with the above conclusion that mitochondria partially maintain their Δψ in the presence of FCCP in our experiments. Additionally, FCCP-induced Δψ depolarization and ensuing inhibition of ATP generation might impair plasma membrane ion balance, leading to (partial) ΔV depolarization and a loss of TMRM from the cell. The latter might be accelerated by the fact that extracellular TMRM was absent during FCCP experiments.

4.2. Performance of TMRM and MTs for mitochondrial morphology quantification

Automated quantification of mitochondrial morphology parameters was feasible in the absence but not in the presence of FCCP (Fig. 3). The latter reflects the inability of our algorithm to segment mitochondria when the difference between mitochondria-specific and aspecific signals is relatively small (*i.e.* when Δψ is substantially depolarized). In the absence of FCCP, mitochondrial morphology parameters were virtually identical for TMRM- and MT-stained cells (Table 2). The mitochondrial mass (*Mm*) ranged between 22,976 (MDR) and 25,079 pixels (CMH2Xros), the number of mitochondrial objects per cell (*Nc*) between 210 (MDR) and 385 (CMH2Xros), the area (size) of these objects (*Am*) between 67 (TMRM, CMH2Xros) and 113 pixels (MDR), the aspect ratio (*AR*) between 2.76 (CMH2Xros) and 3.52 (MDR), and the formfactor (*F*) between 2.64 (CHMH2Xros) and 3.80 (MDR). Statistical evaluation demonstrated that *Mm* was similar for all dyes, whereas *Nc*, *Am*, *AR* and *F* differed for MDR (Fig. 4). Linear regression analysis demonstrated that all morphology parameters significant correlated with mitochondrial fluorescence staining intensity (*Dm*), indicating that the high intensity staining for MDR is likely responsible for this observation (Supplementary Fig. S2). In previous analyses of cell line #5120, mitochondrial morphology was quantified using R123, TMRM and mitochondria-targeted fluorescent proteins [27–31,86]. This yielded a range of TMRM-based "reference" values for *Nc* (between 50 and 150), *AR* (2, 3) and *F* (3–6; [22]). In case of TMRM (Table 1) we here obtained values for *F* (2.71) and *AR* (3.00) relatively close to these reference values, whereas *Nc* (374.2) was substantially higher. This difference is likely due to the use of different microscopy systems, image acquisition settings and/or staining protocols, affecting *Dm*, and thereby morphology parameter values ([22]; Supplementary Fig. S2).

4.3. Δψ-sensitivity of TMRM and MG during photo-induced Δψ flickering

To gain additional insight into the Δψ sensitivity of mitochondrial TMRM and MG staining (representing extremes in FCCP sensitivity; Fig. 2E), the behaviour of these dyes during reversible Δψ depolarizations ("Δψ flickering") was studied (Figs. 5–8). Compatible with the observed FCCP effects, detectable Δψ depolarizations were present and absent in TMRM and MG fluorescence images, respectively (Fig. 6C). Detailed analysis of two closely juxtaposed mitochondria (Mito1, Mito2) during a single Δψ flickering event revealed antiparallel changes in TMRM fluorescence (Fig. 7A–B). These consisted of a tri-phasic TMRM release/uptake in Mito1 mirrored by a tri-phasic TMRM uptake/release in Mito2 (Fig. 7C). Overall, the Δψ flickering event had a duration of ~44 s, displaying a depolarization phase I (~8 s), a stationary phase II (~12 s) and a repolarization phase III (~24 s). Similar kinetics were predicted by a minimal mass action-based mathematical model (Fig. 8A), which assumed that TMRM redistribution was caused by an acute Δψ depolarization of 20 s followed by a linear Δψ repolarisation of 20 s (Fig. 8C). In the model, the Δψ of Mito2 was kept constant, meaning that its TMRM uptake is solely driven by the outside (cytosolic) TMRM concentration ($[TMRM]_c$). This behaviour is compatible with [Eq. (I)], which predicts that more TMRM will accumulate in the mitochondrial matrix of Mito2 (*i.e.* C_m will be higher), when C_{cyt} increases at a constant Δψ. Our experimental data (Figs. 7C and 8G; green symbols) and modelling results (Fig. 8E), strongly suggest that TMRM transfer from Mito1 to Mito2 is relatively fast since $[TMRM]_c$ remained virtually unchanged during the Δψ flickering event. Regarding Δψ flickering dynamics the current data is quantitatively compatible with experimental results in ventricular myocytes, displaying a fast (~9 s or less) depolarization and a half time of recovery of 20–30 s [80]. Although to a lower extent than R123, TMRM was demonstrated to bind to mitochondria and inhibit mitochondrial function in isolated rat heart mitochondria [25]. However, TMRM binding was not required in our minimal model to adequately describe our experimental data (Fig. 8G). This is likely due to the low extracellular TMRM concentration employed in this study (15 nM), and the fact that mitochondrial TMRM accumulation progressively deviates from the Nernst equation (*i.e.* [Eq. (I)]) with increasing cytosolic TMRM concentration [25]. The low extracellular TMRM concentration also makes it unlikely that TMRM inhibits mitochondrial (state 3) respiration in our experiments [25]. Taken together, the Δψ flickering analysis supports the conclusion that: (1) the different kinetic phases of the Δψ flickering event represent a rapid Δψ depolarization (phase I) followed by a slower, ETC-dependent, Δψ repolarization (phase III), and (2) during Δψ flickering TMRM, but not MG, is transferred from Mito1 to Mito2. These findings support the application of combined TMRM/MG staining during Δψ flickering events [62], allowing simultaneous analysis of mitochondrial morphology parameters (MG signal) and Δψ (TMRM signal).

5. Conclusion

In summary, this study demonstrates that the mitochondrial localization of TMRM and MTs is differentially sensitive to Δψ depolarization and that staining with these dyes allows quantitative analysis of mitochondrial morphology parameters. However, even when obtained using the same microscope hardware/settings and image quantification protocol, data obtained with TMRM and MTs cannot be used interchangeably. In this sense, comparison of mitochondrial morphology data between different conditions should be performed using an identical experimental strategy (*e.g.* dye, staining protocol, medium, microscope hardware/settings). It is advised to always including the same control cell line on each experimental day allowing (on-demand) data normalization and quality control analysis [22]. Regarding dye performance, this study provides evidence that TMRM is better suited for integrated analysis of Δψ and/or mitochondrial morphology than the tested MTs under conditions that Δψ is not substantially depolarized.

Supplementary data to this article can be found online at https://doi.org/10.1016/j.bbabio.2023.149027.

CRediT authorship contribution statement

EvdW, **SL** and **AP** performed the experiments. **SD**, **SG**, **EvdW**, **SL**, **AP** and **WJHK** performed data analysis. **ZG** and **WJHK** performed the mathematical modelling. **SG**, **JHMP**, **MJWAH** and **WJHK** supervised the research. All authors contributed to manuscript writing and data interpretation.

Declaration of competing interest

The authors declare the following financial interests/personal relationships which may be considered as potential competing interests: **WJHK** is an *ad-hoc* scientific advisor of Khondrion B.V. (Nijmegen, The Netherlands). This SME had no involvement in the data collection, analysis and interpretation, writing of the manuscript, and in the decision to submit the manuscript for publication.

Data availability

Data will be made available on request.

Acknowledgements

This research was supported by the Innovative Medicines Initiative 2 Joint Undertaking ("PD-MitoQUANT"; Grant Agreement No. 821522) and the Centres for Systems Biology Research initiative (CSBR09/013V) of NWO (The Netherlands Organisation for Scientific Research). **ZG** and **WJHK** were supported by the Next Level Animal Sciences (NLAS) initiative ("Data and Models") of the Wageningen University (Wageningen, The Netherlands). **WJHK** was supported by Radboudumc Principal Investigator (PI) funding (Nijmegen, The Netherlands). We thank Felix Distelmaier, Peter Smittenaar, Harm Huismans and Elianne Bulthuis (Dept. of Biochemistry 286, Radboudumc) for initial experiments.

References

[1] J.A.M. Smeitink, L. van den Heuvel, S. DiMauro, The genetics and pathology of oxidative phosphorylation, Nat. Rev. Genet. 2 (5) (May, 2001) 342–352, https://doi.org/10.1038/35072063 (PMID: 11331900).

[2] L.D. Zorova, V.A. Popkov, E.Y. Plotnikov, D.N. Silachev, I.B. Pevzner, S. S. Jankauskas, V.A. Babenko, S.D. Zorov, A.V. Balakireva, M. Juhaszova, S. J. Sollott, D.B. Zorov, Mitochondrial membrane potential, Anal. Biochem. 552 (Jul 1, 2018) 50–59, https://doi.org/10.1016/j.ab.2017.07.009 (Epub 2017 Jul 12. PMID: 28711444; PMCID: PMC5792320).

[3] P. Mitchell, Coupling of phosphorylation to electron and hydrogen transfer by a chemi-osmotic type of mechanism, Nature 191 (Jul 8, 1961) 144–148, https://doi.org/10.1038/191144a0 (PMID: 13771349).

[4] J.E. Walker, The ATP synthase: the understood, the uncertain and the unknown, Biochem. Soc. Trans. 41 (1) (Feb 1, 2013) 1–16, https://doi.org/10.1042/BST20110773 (PMID: 23356252).

[5] N.C. Price, R.A. Dwek, R.G. Ratcliffe, M.R. Wormald, Principles and Problems in Physical Chemistry for Biochemists, 3rd ed., Oxford University Press, Oxford, UK, 2001.

[6] G. Solaini, G. Sgarbi, G. Lenaz, A. Baracca, Evaluating mitochondrial membrane potential in cells, Biosci. Rep. 27 (1–3) (Jun 2007) 11–21, https://doi.org/10.1007/s10540-007-9033-4 (PMID: 17497220).

[7] D.G. Nicholls, M.W. Ward, Mitochondrial membrane potential and neuronal glutamate excitotoxicity: mortality and millivolts, Trends Neurosci. 23 (4) (Apr 2000) 166–174, https://doi.org/10.1016/s0166-2236(99)01534-9 (PMID: 10717676).

[8] A.B. Bakare, F. Meshrkey, B. Lowe, C. Molder, R.R. Rao, J. Zhan, S. Iyer, MitoCellPhe reveals mitochondrial morphologies in single fibroblasts and clustered stem cells, Am. J. Physiol. Cell Physiol. 321 (4) (Oct 1, 2021) C735–C748, https://doi.org/10.1152/ajpcell.00231.2021 (Epub 2021 Sep 1. PMID: 34469204; PMCID: PMC8560386).

[9] A.B. Bakare, J. Daniel, J. Stabach, A. Rojas, A. Bell, B. Henry, S. Iyer, Quantifying mitochondrial dynamics in patient fibroblasts with multiple developmental defects and mitochondrial disorders, Int. J. Mol. Sci. 22 (12) (Jun 10, 2021) 6263, https://doi.org/10.3390/ijms22126263 (PMID: 34200828; PMCID: PMC8230542).

[10] G. Benard, R. Rossignol, Ultrastructure of the mitochondrion and its bearing on function and bioenergetics, Antioxid. Redox Signal. 10 (8) (Aug 2008) 1313–1342, https://doi.org/10.1089/ars.2007.2000 (PMID: 18435594).

[11] E.P. Bulthuis, M.J.W. Adjobo-Hermans, P.H.G.M. Willems, W.J.H. Koopman, Mitochondrial morphofunction in mammalian cells, Antioxid. Redox Signal. 30 (18) (Jun 20, 2019) 2066–2109, https://doi.org/10.1089/ars.2018.7534 (Epub 2018 Nov 29).

[12] H. Chen, S.A. Detmer, A.J. Ewald, E.E. Griffin, S.E. Fraser, D.C. Chan, Mitofusins Mfn1 and Mfn2 coordinately regulate mitochondrial fusion and are essential for embryonic development, J. Cell Biol. 160 (2) (Jan 20, 2003) 189–200, https://doi.org/10.1083/jcb.200211046 (Epub 2003 Jan 13. PMID: 12527753; PMCID: PMC2172648).

[13] H. Chen, A. Chomyn, D.C. Chan, Disruption of fusion results in mitochondrial heterogeneity and dysfunction, J. Biol. Chem. 280 (28) (Jul 15, 2005) 26185–26192, https://doi.org/10.1074/jbc.M503062200 (Epub 2005 May 17. PMID: 15899901).

[14] T.J. Collins, M.D. Bootman, Mitochondria are morphologically heterogeneous within cells, J. Exp. Biol. 206 (Pt 12) (Jun 2003) 1993–2000, https://doi.org/10.1242/jeb.00244 (PMID: 12756281).

[15] P.H.G.M. Willems, R. Rossignol, C.E. Dieteren, M.P. Murphy, W.J.H. Koopman, Redox homeostasis and mitochondrial dynamics, Cell Metab. 22 (2) (Aug 4, 2015) 207–218, https://doi.org/10.1016/j.cmet.2015.06.006 (Epub 2015 Jul 9. PMID: 26166745).

[16] C. Cottet-Rousselle, X. Ronot, X. Leverve, J.F. Mayol, Cytometric assessment of mitochondria using fluorescent probes, Cytometry A 79 (6) (Jun 2011) 405–425, https://doi.org/10.1002/cyto.a.21061 (PMID: 21595013).

[17] S.W. Perry, J.P. Norman, J. Barbieri, E.B. Brown, H.A. Gelbard, Mitochondrial membrane potential probes and the proton gradient: a practical usage guide, Biotechniques 50 (2) (Feb 2011) 98–115, https://doi.org/10.2144/000113610 (PMID: 21486251; PMCID: PMC3115691).

[18] G. Clutton, K. Mollan, M. Hudgens, N. Goonetilleke, A reproducible, objective method using MitoTracker® fluorescent dyes to assess mitochondrial mass in T cells by flow cytometry, Cytometry A 95 (4) (Apr 2019) 450–456, https://doi.org/10.1002/cyto.a.23705 (Epub 2018 Dec 21).

[19] C.J. Feeney, P.S. Pennefather, A.V. Gyulkhandanyan, A cuvette-based fluorometric analysis of mitochondrial membrane potential measured in cultured astrocyte monolayers, J. Neurosci. Methods 125 (1–2) (May 30, 2003) 13–25, https://doi.org/10.1016/s0165-0270(03)00027-x (PMID: 12763226).

[20] D. Floryk, J. Houstěk, Tetramethyl rhodamine methyl ester (TMRM) is suitable for cytofluorometric measurements of mitochondrial membrane potential in cells treated with digitonin, Biosci. Rep. 19 (1) (Feb 1999) 27–34, https://doi.org/10.1023/a:1020193906974 (PMID: 10379904).

[21] N. Gautam, S. Sankaran, J.A. Yason, K.S.W. Tan, N.R.J. Gascoigne, A high content imaging flow cytometry approach to study mitochondria in T cells: MitoTracker Green FM dye concentration optimization, Methods 134–135 (Feb 1, 2018) 11–19, https://doi.org/10.1016/j.ymeth.2017.11.015 (Epub 2017 Dec 2. PMID: 29198814).

[22] E.F. Iannetti, J.A.M. Smeitink, J. Beyrath, P.H.G.M. Willems, W.J.H. Koopman, Multiplexed high-content analysis of mitochondrial morphofunction using live-cell microscopy, Nat. Protoc. 11 (9) (Sep 2016) 1693–1710, https://doi.org/10.1038/nprot.2016.094 (Epub 2016 Aug 18. PMID: 27560174).

[23] S. Jayaraman, Flow cytometric determination of mitochondrial membrane potential changes during apoptosis of T lymphocytic and pancreatic beta cell lines: comparison of tetramethylrhodamineethylester (TMRE), chloromethyl-X-rosamine (H2-CMX-Ros) and MitoTracker Red 580 (MTR580), J. Immunol. Methods 306 (1–2) (Nov 30, 2005) 68–79, https://doi.org/10.1016/j.jim.2005.07.024 (Epub 2005 Sep 29. PMID: 16256133).

[24] J. Plásek, A. Vojtísková, J. Houstek, Flow-cytometric monitoring of mitochondrial depolarisation: from fluorescence intensities to millivolts, J. Photochem. Photobiol. B 78 (2) (Feb 1, 2005) 99–108, https://doi.org/10.1016/j.jphotobiol.2004.09.011 (PMID: 15664496).

[25] R.C. Scaduto Jr., L.W. Grotyohann, Measurement of mitochondrial membrane potential using fluorescent rhodamine derivatives, Biophys. J. 76 (1 Pt 1) (Jan 1999) 469–477, https://doi.org/10.1016/S0006-3495(99)77214-0 (PMID: 9876159; PMCID: PMC1302536).

[26] E.P. Bulthuis, C. Einer, F. Distelmaier, L. Groh, S.E. van Emst-de Vries, E. van de Westerlo, M. van de Wal, J. Wagenaars, R.J. Rodenburg, J.A.M. Smeitink, N. P. Riksen, P.H.G.M. Willems, M.J.W. Adjobo-Hermans, H. Zischka, W.J. H. Koopman, The decylTPP mitochondria-targeting moiety lowers electron transport chain supercomplex levels in primary human skin fibroblasts, Free Radic. Biol. Med. 188 (Aug 1, 2022) 434–446, https://doi.org/10.1016/j.freeradbiomed.2022.06.011 (Epub 2022 Jun 17. PMID: 35718301).

[27] F. Distelmaier, W.J.H. Koopman, E.R. Testa, A.S. de Jong, H.G. Swarts, E. Mayatepek, J.A. Smeitink, P.H. Willems, Life cell quantification of mitochondrial membrane potential at the single organelle level, Cytometry A 73 (2) (Feb 2008) 129–138, https://doi.org/10.1002/cyto.a.20503 (PMID: 18163486).

[28] W.J.H. Koopman, S. Verkaart, H.J. Visch, F.H. van der Westhuizen, M.P. Murphy, L.W. van den Heuvel, J.A. Smeitink, P.H. Willems, Inhibition of complex I of the electron transport chain causes $O_2^{\bullet-}$-mediated mitochondrial outgrowth, Am. J. Physiol. Cell Physiol. 288 (6) (Jun 2005) C1440–C1450, https://doi.org/10.1152/ajpcell.00607.2004 (Epub 2005 Jan 12. PMID: 15647387).

[29] W.J.H. Koopman, H.J. Visch, S. Verkaart, L.W. van den Heuvel, J.A. Smeitink, P. H. Willems, Mitochondrial network complexity and pathological decrease in complex I activity are tightly correlated in isolated human complex I deficiency, Am. J. Physiol. Cell Physiol. 289 (4) (Oct 2005) C881–C890, https://doi.org/10.1152/ajpcell.00104.2005 (Epub 2005 May 18).

[30] W.J.H. Koopman, H.J. Visch, J.A. Smeitink, P.H. Willems, Simultaneous quantitative measurement and automated analysis of mitochondrial morphology, mass, potential, and motility in living human skin fibroblasts, Cytometry A 69 (1) (Jan 2006) 1–12, https://doi.org/10.1002/cyto.a.20198 (PMID: 16342116).

[31] W.J.H. Koopman, F. Distelmaier, J.J. Esseling, J.A. Smeitink, P.H. Willems, Computer-assisted live cell analysis of mitochondrial membrane potential, morphology and calcium handling, Methods 46 (4) (Dec 2008) 304–311, https://doi.org/10.1016/j.ymeth.2008.09.018 (Epub 2008 Oct 16. PMID: 18929665).

[32] J. Teixeira, F. Basit, P.H.G.M. Willems, J.A. Wagenaars, E. van de Westerlo, R. Amorim, F. Cagide, S. Benfeito, C. Oliveira, F. Borges, P.J. Oliveira, W.J. H. Koopman, Mitochondria-targeted phenolic antioxidants induce ROS-protective pathways in primary human skin fibroblasts, Free Radic. Biol. Med. 163 (Feb 1, 2021) 314–324, https://doi.org/10.1016/j.freeradbiomed.2020.12.023 (Epub 2020 Dec 29. PMID: 33359686).

[33] P.H.G.M. Willems, J.A.M. Smeitink, W.J.H. Koopman, Mitochondrial dynamics in human NADH:ubiquinone oxidoreductase deficiency, Int. J. Biochem. Cell Biol. 41 (10) (Oct 2009) 1773–1782, https://doi.org/10.1016/j.biocel.2009.01.012 (Epub 2009 Jan 28. PMID: 19703648).

[34] B. Ehrenberg, V. Montana, M.D. Wei, J.P. Wuskell, L.M. Loew, Membrane potential can be determined in individual cells from the nernstian distribution of cationic dyes, Biophys. J. 53 (5) (May 1988) 785–794, https://doi.org/10.1016/S0006-3495(88)83158-8 (PMID: 3390520; PMCID: PMC1330255).

[35] S. Goldstein, L.B. Korczack, Status of mitochondria in living human fibroblasts during growth and senescence in vitro: use of the laser dye rhodamine 123, J. Cell Biol. 91 (2 Pt 1) (Nov 1981) 392–398, https://doi.org/10.1083/jcb.91.2.392 (PMID: 7309788; PMCID: PMC2111971).

[36] L.V. Johnson, M.L. Walsh, L.B. Chen, Localization of mitochondria in living cells with rhodamine 123, Proc. Natl. Acad. Sci. U. S. A. 77 (2) (Feb 1980) 990–994, https://doi.org/10.1073/pnas.77.2.990 (PMID: 6965798; PMCID: PMC348409).

[37] J.J. Lemasters, V.K. Ramshesh, Imaging of mitochondrial polarization and depolarization with cationic fluorophores, Methods Cell Biol. 80 (2007) 283–295, https://doi.org/10.1016/S0091-679X(06)80014-2 (PMID: 17445700).

[38] M.F. Ross, G.F. Kelso, F.H. Blaikie, A.M. James, H.M. Cochemé, A. Filipovska, T. Da Ros, T.R. Hurd, R.A. Smith, M.P. Murphy, Lipophilic triphenylphosphonium cations as tools in mitochondrial bioenergetics and free radical biology, Biochemistry (Mosc) 70 (2) (Feb 2005) 222–230, https://doi.org/10.1007/s10541-005-0104-5 (PMID: 15807662).

[39] F. Sivandzade, A. Bhalerao, L. Cucullo, Analysis of the mitochondrial membrane potential using the cationic JC-1 dye as a sensitive fluorescent probe, Bio-Protoc. 9 (1) (Jan 5, 2019) e3128, https://doi.org/10.21769/BioProtoc.3128 (PMID: 30687773; PMCID: PMC6343665).

[40] C. Mao, W.S. Kisaalita, Determination of resting membrane potential of individual neuroblastoma cells (IMR-32) using a potentiometric dye (TMRM) and confocal microscopy, J. Fluoresc. 14 (6) (Nov 2004) 739–743, https://doi.org/10.1023/b:jofl.0000047224.41328.f8 (PMID: 15649026).

[41] D.L. Farkas, M.D. Wei, P. Febbroriello, J.H. Carson, L.M. Loew, Simultaneous imaging of cell and mitochondrial membrane potentials, Biophys. J. 56 (6) (Dec 1989) 1053–1069, https://doi.org/10.1016/S0006-3495(89)82754-7 (Erratum in: Biophys J 1990 Mar;57(3):following 684. PMID: 2611324; PMCID: PMC1280610).

[42] D.G. Nicholls, Simultaneous monitoring of ionophore- and inhibitor-mediated plasma and mitochondrial membrane potential changes in cultured neurons, J. Biol. Chem. 281 (21) (May 26 2006) 14864–14874, https://doi.org/10.1074/jbc.M510916200 (Epub 2006 Mar 21. PMID: 16551630).

[43] M. Forkink, G.R. Manjeri, D.C. Liemburg-Apers, E. Nibbeling, M. Blanchard, A. Wojtala, J.A. Smeitink, M.R. Wieckowski, P.H. Willems, W.J.H. Koopman, Mitochondrial hyperpolarization during chronic complex I inhibition is sustained by low activity of complex II, III, IV and V, Biochim. Biophys. Acta 1837 (8) (Aug 2014) 1247–1256, https://doi.org/10.1016/j.bbabio.2014.04.008 (Epub 2014 Apr 24. PMID: 24769419).

[44] M.P. Murphy, R.A. Smith, Drug delivery to mitochondria: the key to mitochondrial medicine, Adv. Drug Deliv. Rev. 41 (2) (Mar 30, 2000) 235–250, https://doi.org/10.1016/s0169-409x(99)00069-1 (PMID: 10699318).

[45] M. Poot, Y.Z. Zhang, J.A. Krämer, K.S. Wells, L.J. Jones, D.K. Hanzel, A.G. Lugade, V.L. Singer, R.P. Haugland, Analysis of mitochondrial morphology and function with novel fixable fluorescent stains, J. Histochem. Cytochem. 44 (12) (Dec 1996) 1363–1372, https://doi.org/10.1177/44.12.8985128 (PMID: 8985128).

[46] R.P. Haugland, Handbook of Fluorescent Probes and Research Chemicals, Molecular Probes, Inc., Eugene, Oregon, 1999.

[47] K. Gilmore, M. Wilson, The use of chloromethyl-X-rosamine (Mitotracker red) to measure loss of mitochondrial membrane potential in apoptotic cells is incompatible with cell fixation, Cytometry 36 (4) (Aug 1, 1999) 355–358, https://doi.org/10.1002/(sici)1097-0320(19990801)36:4<355::aid-cyto11>3.0.co;2-9 (PMID: 10404152).

[48] J.F. Buckman, H. Hernández, G.J. Kress, T.V. Votyakova, S. Pal, I.J. Reynolds, MitoTracker labeling in primary neuronal and astrocytic cultures: influence of mitochondrial membrane potential and oxidants, J. Neurosci. Methods 104 (2) (Jan 15, 2001) 165–176, https://doi.org/10.1016/s0165-0270(00)00340-x (PMID: 11164242).

[49] F. Basit, L.M. van Oppen, L. Schöckel, H.M. Bossenbroek, S.E. van Emst-de Vries, J. C. Hermeling, S. Grefte, C. Kopitz, M. Heroult, P. Hgm Willems, W.J.H. Koopman, Mitochondrial complex I inhibition triggers a mitophagy-dependent ROS increase leading to necroptosis and ferroptosis in melanoma cells, Cell Death Dis. 8 (3) (Mar 30, 2017) e2716, https://doi.org/10.1038/cddis.2017.133 (PMID: 28358377; PMCID: PMC5386536).

[50] L. Buhlman, M. Damiano, G. Bertolin, R. Ferrando-Miguel, A. Lombès, A. Brice, O. Corti, Functional interplay between Parkin and Drp1 in mitochondrial fission and clearance, Biochim. Biophys. Acta 1843 (9) (Sep 2014) 2012–2026, https://doi.org/10.1016/j.bbamcr.2014.05.012 (Epub 2014 May 27. PMID: 24878071).

[51] L.F. Burbulla, C. Schelling, H. Kato, D. Rapaport, D. Woitalla, C. Schiesling, C. Schulte, M. Sharma, T. Illig, P. Bauer, S. Jung, A. Nordheim, L. Schöls, O. Riess, R. Krüger, Dissecting the role of the mitochondrial chaperone mortalin in Parkinson's disease: functional impact of disease-related variants on mitochondrial homeostasis, Hum. Mol. Genet. 19 (22) (Nov 15, 2010) 4437–4452, https://doi.org/10.1093/hmg/ddq370 (Epub 2010 Sep 2. PMID: 20817635; PMCID: PMC3298849).

[52] T. Grau, L.F. Burbulla, G. Engl, C. Delettre, B. Delprat, K. Oexle, B. Leo-Kottler, T. Roscioli, R. Krüger, D. Rapaport, B. Wissinger, S. Schimpf-Linzenbold, A novel heterozygous OPA3 mutation located in the mitochondrial target sequence results in altered steady-state levels and fragmented mitochondrial network, J. Med. Genet. 50 (12) (Dec 2013) 848–858, https://doi.org/10.1136/jmedgenet-2013-101774 (Epub 2013 Oct 17. PMID: 24136862).

[53] K.J. Tronstad, M. Nooteboom, L.I. Nilsson, J. Nikolaisen, M. Sokolewicz, S. Grefte, I.K. Pettersen, S. Dyrstad, F. Hoel, P.H. Willems, W.J.H. Koopman, Regulation and quantification of cellular mitochondrial morphology and content, Curr. Pharm. Des. 20 (35) (2014) 5634–5652, https://doi.org/10.2174/1381612820666140305230546 (PMID: 24606803).

[54] R.O. Vogel, R.J. Janssen, M.A. van den Brand, C.E. Dieteren, S. Verkaart, W.J. H. Koopman, P.H. Willems, W. Pluk, L.P. van den Heuvel, J.A. Smeitink, L. G. Nijtmans, Cytosolic signaling protein Ecsit also localizes to mitochondria where it interacts with chaperone NDUFAF1 and functions in complex I assembly, Genes Dev. 21 (5) (Mar 1, 2007) 615–624, https://doi.org/10.1101/gad.408407 (PMID: 17344420; PMCID: PMC1820902).

[55] T. Yu, J.L. Robotham, Y. Yoon, Increased production of reactive oxygen species in hyperglycemic conditions requires dynamic change of mitochondrial morphology, Proc. Natl. Acad. Sci. U. S. A. 103 (8) (Feb 21, 2006) 2653–2658, https://doi.org/10.1073/pnas.0511154103 (Epub 2006 Feb 13. PMID: 16477035; PMCID: PMC1413838).

[56] H. Zhang, H.M. Huang, R.C. Carson, J. Mahmood, H.M. Thomas, G.E. Gibson, Assessment of membrane potentials of mitochondrial populations in living cells, Anal. Biochem. 298 (2) (Nov 15, 2001) 170–180, https://doi.org/10.1006/abio.2001.5348 (PMID: 11757503).

[57] H. Dong, S.H. Cheung, Y. Liang, B. Wang, R. Ramalingam, P. Wang, H. Sun, S. H. Cheng, Y.W. Lam, "Stainomics": identification of mitotracker labeled proteins in mammalian cells, Electrophoresis 34 (13) (Jul 2013) 1957–1964, https://doi.org/10.1002/elps.201200557 (PMID: 23595693).

[58] S.V. Buravkov, M.V. Pogodina, L.B. Buravkova, Comparison of mitochondrial fluorescent dyes in stromal cells, Bull. Exp. Biol. Med. 157 (5) (Sep 2014) 654–658, https://doi.org/10.1007/s10517-014-2637-3 (Epub 2014 Sep 26. PMID: 25257434).

[59] J.F. Keij, C. Bell-Prince, J.A. Steinkamp, Staining of mitochondrial membranes with 10-nonyl acridine orange, MitoFluor Green, and MitoTracker Green is affected by mitochondrial membrane potential altering drugs, Cytometry 39 (3) (Mar 1, 2000) 203–210, https://doi.org/10.1002/(sici)1097-0320(20000301)39:3<203::aid-cyto5>3.0.co;2-z (PMID: 10685077).

[60] A.I. Mot, J.R. Liddell, A.R. White, P.J. Crouch, Circumventing the Crabtree effect: a method to induce lactate consumption and increase oxidative phosphorylation in cell culture, Int. J. Biochem. Cell Biol. 79 (Oct 2016) 128–138, https://doi.org/10.1016/j.biocel.2016.08.029 (Epub 2016 Aug 30. PMID: 27590850).

[61] W. Pendergrass, N. Wolf, M. Poot, Efficacy of MitoTracker Green and CMXrosamine to measure changes in mitochondrial membrane potentials in living cells and tissues, Cytometry A 61 (2) (Oct 2004) 162–169, https://doi.org/10.1002/cyto.a.20033 (PMID: 15382028).

[62] I. Sambri, F. Massa, F. Gullo, S. Meneghini, L. Cassina, M. Carraro, G. Dina, A. Quattrini, L. Patanella, A. Carissimo, A. Iuliano, F. Santorelli, F. Codazzi, F. Grohovaz, P. Bernardi, A. Becchetti, G. Casari, Impaired flickering of the permeability transition pore causes SPG7 spastic paraplegia, EBioMedicine 61 (Nov 2020) 103050, https://doi.org/10.1016/j.ebiom.2020.103050 (Epub 2020 Oct 9. PMID: 33045469; PMCID: PMC7553352).

[63] M.W. Ward, Quantitative analysis of membrane potentials, Methods Mol. Biol. 591 (2010) 335–351, https://doi.org/10.1007/978-1-60761-404-3_20 (PMID: 19957140).

[64] N. Esteras, M.J.W. Adjobo-Hermans, A.Y. Abramov, W.J.H. Koopman, Visualization of mitochondrial membrane potential in mammalian cells, Methods Cell Biol. 155 (2020) 221–245, https://doi.org/10.1016/bs.mcb.2019.10.003 (Epub 2019 Dec 10. PMID: 32183960).

[65] D. Iyer, R.D. Ray, D. Pappas, High temporal resolution fluorescence measurements of a mitochondrial dye for detection of early stage apoptosis, Analyst 138 (17) (Sep 7, 2013) 4892–4897, https://doi.org/10.1039/c3an01142a (Epub 2013 Jul 8. PMID: 23831722; PMCID: PMC3754438).

[66] L. Scorrano, V. Petronilli, R. Colonna, F. Di Lisa, P. Bernardi, Chloromethyltetramethylrosamine (Mitotracker Orange) induces the mitochondrial permeability transition and inhibits respiratory complex I. Implications for the mechanism of cytochrome c release, J. Biol. Chem. 274 (35) (Aug 27, 1999) 24657–24663, https://doi.org/10.1074/jbc.274.35.24657 (PMID: 10455132).

[67] M. Nooteboom, M. Forkink, P.H.G.M. Willems, W.J.H. Koopman, Live-cell quantification of mitochondrial functional parameters. Chapter 6, in: Badoer E. Neurometh (Ed.), Visualization Techniques: From Immunochemistry to Magnetic Resonance Imaging vol. 70, Springer Science+Business Media, LLC, 2012, pp. 111–127, https://doi.org/10.1007/978-1-61779-897-9_6.

[68] L. Blanchet, S. Grefte, J.A. Smeitink, P.H. Willems, W.J.H. Koopman, Photo-induction and automated quantification of reversible mitochondrial permeability transition pore opening in primary mouse myotubes, PLoS One 9 (11) (Nov 25, 2014) e114090, https://doi.org/10.1371/journal.pone.0114090 (PMID: 25423172; PMCID: PMC4244163).

[69] A.J. de Groof, J.A. Fransen, R.J. Errington, P.H. Willems, B. Wieringa, W.J. H. Koopman, The creatine kinase system is essential for optimal refill of the sarcoplasmic reticulum Ca^{2+} store in skeletal muscle, J. Biol. Chem. 277 (7) (Feb 15, 2002) 5275–5284, https://doi.org/10.1074/jbc.M108157200 (Epub 2001 Dec 4. PMID: 11734556).

[70] P. Bernardi, M. Carraro, G. Lippe, The mitochondrial permeability transition: recent progress and open questions, FEBS J. 289 (22) (Nov 2022) 7051–7074, https://doi.org/10.1111/febs.16254 (Epub 2021 Nov 12. PMID: 34710270; PMCID: PMC9787756).

[71] F. De Giorgi, L. Lartigue, F. Ichas, Electrical coupling and plasticity of the mitochondrial network, Cell Calcium 28 (5–6) (Nov–Dec 2000) 365–370, https://doi.org/10.1054/ceca.2000.0177 (PMID: 11115375).
[72] M.R. Duchen, A. Leyssens, M. Crompton, Transient mitochondrial depolarizations reflect focal sarcoplasmic reticular calcium release in single rat cardiomyocytes, J. Cell Biol. 142 (4) (Aug 24, 1998) 975–988, https://doi.org/10.1083/jcb.142.4.975 (PMID: 9722610; PMCID: PMC2132882).
[73] A.M. Falchi, R. Isola, A. Diana, M. Putzolu, G. Diaz, Characterization of depolarization and repolarization phases of mitochondrial membrane potential fluctuations induced by tetramethylrhodamine methyl ester photoactivation, FEBS J. 272 (7) (Apr 2005) 1649–1659, https://doi.org/10.1111/j.1742-4658.2005.04586.x (PMID: 15794752).
[74] J. Hüser, C.E. Rechenmacher, L.A. Blatter, Imaging the permeability pore transition in single mitochondria, Biophys. J. 74 (4) (Apr 1998) 2129–2137, https://doi.org/10.1016/S0006-3495(98)77920-2 (PMID: 9545072; PMCID: PMC1299554).
[75] J. Hüser, L.A. Blatter, Fluctuations in mitochondrial membrane potential caused by repetitive gating of the permeability transition pore, Biochem. J. 343 (Pt 2) (Oct 15, 1999) 311–317 (PMID: 10510294; PMCID: PMC1220555).
[76] C.M. O'Reilly, K.E. Fogarty, R.M. Drummond, R.A. Tuft, J.V. Walsh Jr., Quantitative analysis of spontaneous mitochondrial depolarizations, Biophys. J. 85 (5) (Nov 2003) 3350–3357, https://doi.org/10.1016/S0006-3495(03)74754-7 (PMID: 14581236; PMCID: PMC1303612).
[77] K.F. Tehrani, E.G. Pendleton, W.M. Southern, J.A. Call, L.J. Mortensen, Two-photon deep-tissue spatially resolved mitochondrial imaging using membrane potential fluorescence fluctuations, Biomed. Opt. Express 9 (1) (Dec 19, 2017) 254–259, https://doi.org/10.1364/BOE.9.000254 (PMID: 29359101; PMCID: PMC5772580).
[78] Y. Uechi, H. Yoshioka, D. Morikawa, Y. Ohta, Stability of membrane potential in heart mitochondria: single mitochondrion imaging, Biochem. Biophys. Res. Commun. 344 (4) (Jun 16, 2006) 1094–1101, https://doi.org/10.1016/j.bbrc.2006.03.233 (Epub 2006 Apr 19. PMID: 16647039).
[79] O. Vergun, T.V. Votyakova, I.J. Reynolds, Spontaneous changes in mitochondrial membrane potential in single isolated brain mitochondria, Biophys. J. 85 (5) (Nov 2003) 3358–3366, https://doi.org/10.1016/S0006-3495(03)74755-9 (PMID: 14581237; PMCID: PMC1303613).
[80] L. Boyman, A.K. Coleman, G. Zhao, A.P. Wescott, H.C. Joca, B.M. Greiser, M. Karbowski, C.W. Ward, W.J. Lederer, Dynamics of the mitochondrial permeability transition pore: transient and permanent opening events, Arch. Biochem. Biophys. 666 (May 15, 2019) 31–39, https://doi.org/10.1016/j.abb.2019.03.016 (Epub 2019 Mar 28. PMID: 30930285; PMCID: PMC6538282).
[81] F. Ricchelli, J. Sileikytė, P. Bernardi, Shedding light on the mitochondrial permeability transition, Biochim. Biophys. Acta 1807 (5) (May 2011) 482–490, https://doi.org/10.1016/j.bbabio.2011.02.012 (Epub 2011 Mar 4. PMID: 21377443).
[82] K. Yalamanchili, N. Afzal, L. Boyman, C.A. Mannella, W.J. Lederer, M.S. Jafri, Understanding the dynamics of the transient and permanent opening events of the mitochondrial permeability transition pore with a novel stochastic model, Membranes (Basel) 12 (5) (Apr 30, 2022) 494, https://doi.org/10.3390/membranes12050494 (PMID: 35629820; PMCID: PMC9146742).
[83] C. Sargiacomo, S. Stonehouse, Z. Moftakhar, F. Sotgia, M.P. Lisanti, MitoTracker Deep Red (MTDR) is a metabolic inhibitor for targeting mitochondria and eradicating cancer stem cells (CSCs), with anti-tumor and anti-metastatic activity in vivo, Front. Oncol. 11 (Jul 30, 2021) 678343, https://doi.org/10.3389/fonc.2021.678343 (PMID: 34395247; PMCID: PMC8361836).
[84] F. Legros, A. Lombès, P. Frachon, M. Rojo, Mitochondrial fusion in human cells is efficient, requires the inner membrane potential, and is mediated by mitofusins, Mol. Biol. Cell 13 (12) (Dec 2002) 4343–4354, https://doi.org/10.1091/mbc.e02-06-0330 (PMID: 12475957; PMCID: PMC138638).
[85] J.P. Brennan, R.G. Berry, M. Baghai, M.R. Duchen, M.J. Shattock, FCCP is cardioprotective at concentrations that cause mitochondrial oxidation without detectable depolarisation, Cardiovasc. Res. 72 (2) (Nov 1, 2006) 322–330, https://doi.org/10.1016/j.cardiores.2006.08.006 (Epub 2006 Aug 16. PMID: 16979603).
[86] W.J.H. Koopman, M.A. Hink, S. Verkaart, H.J. Visch, J.A. Smeitink, P.H. Willems, Partial complex I inhibition decreases mitochondrial motility and increases matrix protein diffusion as revealed by fluorescence correlation spectroscopy, Biochim. Biophys. Acta 1767 (7) (Jul 2007) 940–947, https://doi.org/10.1016/j.bbabio.2007.03.013 (Epub 2007 Apr 6. PMID: 17490603).